Since January 2020 Elsevier has created a COVID-19 resource centre with free information in English and Mandarin on the novel coronavirus COVID-19. The COVID-19 resource centre is hosted on Elsevier Connect, the company's public news and information website.

Cell

Visualizing in deceased COVID-19 patients how SARS-CoV-2 attacks the respiratory and olfactory mucosae but spares the olfactory bulb

Graphical abstract

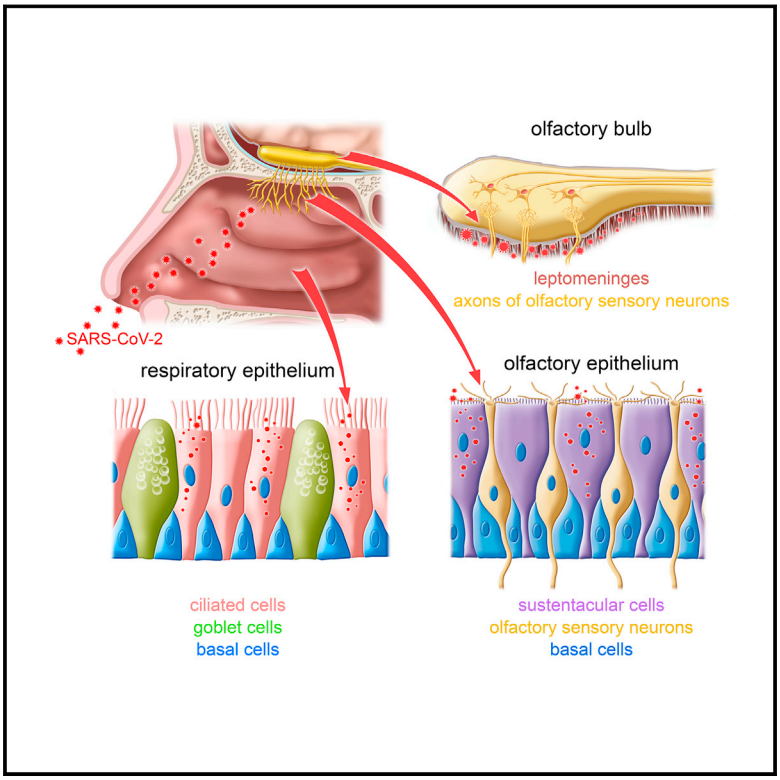

Highlights

- A postmortem bedside surgical procedure was developed for COVID-19 and control patients
- Ciliated cells are the main target cell type for SARS-CoV-2 in the respiratory mucosa
- Sustentacular cells (non-neuronal) are the main target cell type in the olfactory mucosa
- No evidence for infection of olfactory sensory neurons or olfactory bulb parenchyma

Authors

Mona Khan, Seung-Jun Yoo, Marnick Clijsters, ..., Joost Wauters, Peter Mombaerts, Laura Van Gerven

Correspondence

peter.mombaerts@gen.mpg.de (P.M.), laura.vangerven@uzleuven.be (L.V.G.)

In brief

Postmortem samples of respiratory and olfactory mucosa and whole olfactory bulbs are harvested immediately after the death of COVID-19 patients revealing ciliated cells and sustentacular cells but not olfactory sensory neurons as the main target cell types for SARS-CoV-2 infection and replication.

Khan et al., 2021, Cell *184*, 5932–5949
November 24, 2021
https://doi.org/10.1016/j.cell.2021.10.027

CellPress

CellPress
OPEN ACCESS

Cell

Article

Visualizing in deceased COVID-19 patients how SARS-CoV-2 attacks the respiratory and olfactory mucosae but spares the olfactory bulb

Mona Khan,[1,20] Seung-Jun Yoo,[1,20] Marnick Clijsters,[2,21] Wout Backaert,[3,4,21] Arno Vanstapel,[5,21] Kato Speleman,[6] Charlotte Lietaer,[6] Sumin Choi,[1] Tyler D. Hether,[7] Lukas Marcelis,[5] Andrew Nam,[7] Liuliu Pan,[7] Jason W. Reeves,[7] Pauline Van Bulck,[3] Hai Zhou,[1] Marc Bourgeois,[8] Yves Debaveye,[9,10] Paul De Munter,[11,12] Jan Gunst,[9,10] Mark Jorissen,[2,3] Katrien Lagrou,[13,14] Natalie Lorent,[15] Arne Neyrinck,[16,17] Marijke Peetermans,[11,12] Dietmar Rudolf Thal,[5,18] Christophe Vandenbriele,[17,19] Joost Wauters,[11,12] Peter Mombaerts,[1,22,*] and Laura Van Gerven[2,3,4,*]

[1]Max Planck Research Unit for Neurogenetics, Frankfurt, Germany
[2]Department of Neurosciences, Experimental Otorhinolaryngology, Rhinology Research, KU Leuven, Leuven, Belgium
[3]Department of Otorhinolaryngology, Head and Neck Surgery, University Hospitals Leuven, Leuven, Belgium
[4]Department of Microbiology, Immunology and Transplantation, Allergy and Clinical Immunology Research Unit, KU Leuven, Leuven, Belgium
[5]Department of Pathology, University Hospitals Leuven, Leuven, Belgium
[6]Department of Otorhinolaryngology, Head and Neck Surgery, AZ Sint-Jan Brugge-Oostende AV, Bruges, Belgium
[7]NanoString Technologies Inc., Seattle, WA, USA
[8]Department of Anesthesiology and Intensive Care Medicine, AZ Sint-Jan Brugge-Oostende AV, Bruges, Belgium
[9]Intensive Care Medicine, University Hospitals Leuven, Leuven, Belgium
[10]Department of Cellular and Molecular Medicine, Laboratory of Intensive Care Medicine, KU Leuven, Leuven, Belgium
[11]Department of General Internal Medicine, University Hospitals Leuven, Leuven, Belgium
[12]Department of Microbiology, Immunology and Transplantation, Laboratory for Clinical Infectious and Inflammatory Disorders, KU Leuven, Leuven, Belgium
[13]Department of Laboratory Medicine and National Reference Centre for Respiratory Pathogens, University Hospitals Leuven, Leuven, Belgium
[14]Department of Microbiology, Immunology and Transplantation, Laboratory of Clinical Bacteriology and Mycology, KU Leuven, Leuven, Belgium
[15]Department of Respiratory Diseases, University Hospitals Leuven, Leuven, Belgium
[16]Department of Anesthesia, University Hospitals Leuven, Leuven, Belgium
[17]Department of Cardiovascular Sciences, KU Leuven, Leuven, Belgium
[18]Department of Imaging and Pathology, Laboratory of Neuropathology and Leuven Brain Institute, KU Leuven, Leuven, Belgium
[19]Department of Cardiovascular Diseases, University Hospitals Leuven, Leuven, Belgium
[20]These authors contributed equally
[21]These authors contributed equally
[22]Lead contact
*Correspondence: peter.mombaerts@gen.mpg.de (P.M.), laura.vangerven@uzleuven.be (L.V.G.)
https://doi.org/10.1016/j.cell.2021.10.027

SUMMARY

Anosmia, the loss of smell, is a common and often the sole symptom of COVID-19. The onset of the sequence of pathobiological events leading to olfactory dysfunction remains obscure. Here, we have developed a post-mortem bedside surgical procedure to harvest endoscopically samples of respiratory and olfactory mucosae and whole olfactory bulbs. Our cohort of 85 cases included COVID-19 patients who died a few days after infection with SARS-CoV-2, enabling us to catch the virus while it was still replicating. We found that sustentacular cells are the major target cell type in the olfactory mucosa. We failed to find evidence for infection of olfactory sensory neurons, and the parenchyma of the olfactory bulb is spared as well. Thus, SARS-CoV-2 does not appear to be a neurotropic virus. We postulate that transient insufficient support from sustentacular cells triggers transient olfactory dysfunction in COVID-19. Olfactory sensory neurons would become affected without getting infected.

INTRODUCTION

Olfactory dysfunction was recognized early in the COVID-19 pandemic (Eliezer et al., 2020; Lüers et al., 2020; Vaira et al., 2020b) and is a strong and consistent symptom associated with a positive COVID-19 test (Sudre et al., 2021). Well into the second year of the pandemic (Wang et al., 2020), there is no explanation in sight as to how SARS-CoV-2 mutes or alters the

A

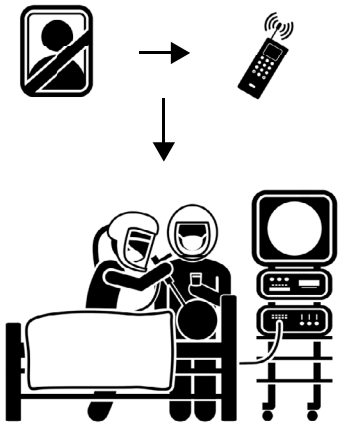

B

	Total n=68		ICU n=37		Ward n=31	
Age	80	69–85	71	62–80	85	82–89
Men	48	71%	28	76%	20	65%
Medical history						
Obesity or overweight	44	65%	30	81%	14	45%
Diabetes mellitus type 2	30	44%	17	46%	13	42%
Hypertension	50	74%	27	73%	23	74%
Chronic kidney disease	24	35%	8	22%	16	52%
Cardiovascular disease	44	65%	21	57%	23	74%
Chronic lung disease	26	38%	15	41%	11	35%
Smoking	9	13%	7	19%	2	6%
Immunocompromised state	26	38%	15	41%	11	35%
COVID-19 diagnosis by PCR						
≤ 7 days prior to death	13	19%	5	14%	8	26%
> 7 and ≤ 14 days	26	38%	7	19%	19	61%
> 14 and ≤ 21 days	8	12%	4	11%	4	13%
> 21 and ≤ 28 days	7	10%	7	19%	0	0%
> 28 days	14	21%	14	38%	0	0%
Days of symptoms before hospitalization	5	1–7	6	3–8	2	1–5
Days on COVID-19 ICU/ward	11	6–22	21	13–32	8	5–10
Highest SOFA score	14	11–17	14	11–17		
Postmortem interval in minutes	71	53–100	67	44–89	85	65–136
Duration of procedure in minutes	58	43–79	54	42–71	60	47–118

C

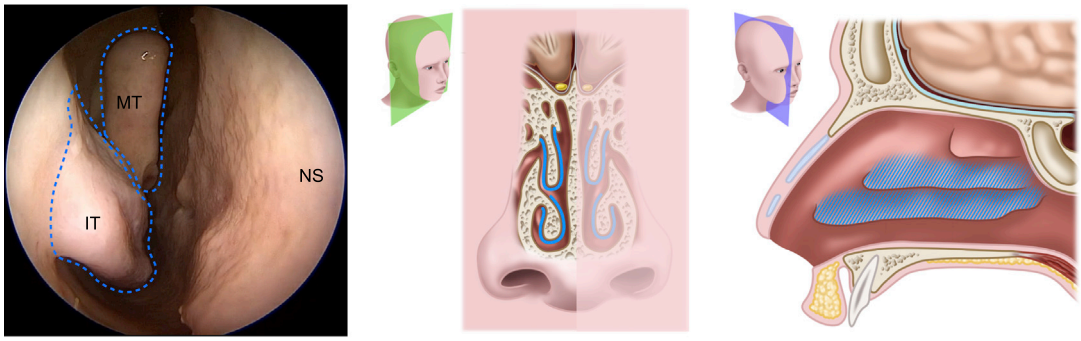

D

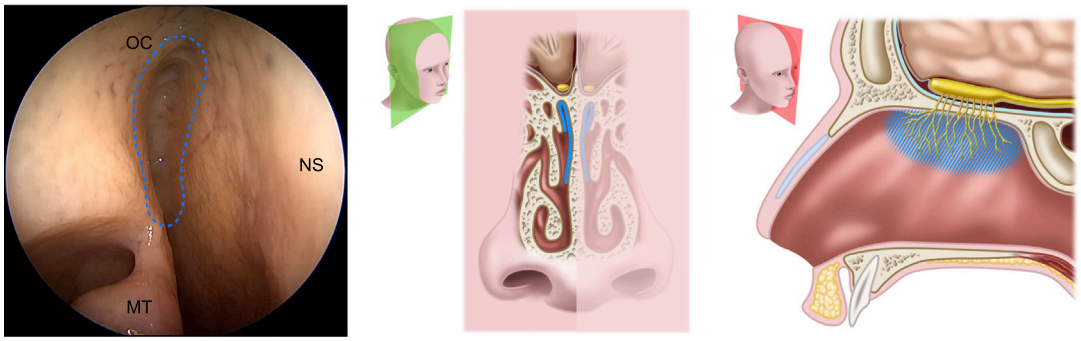

E

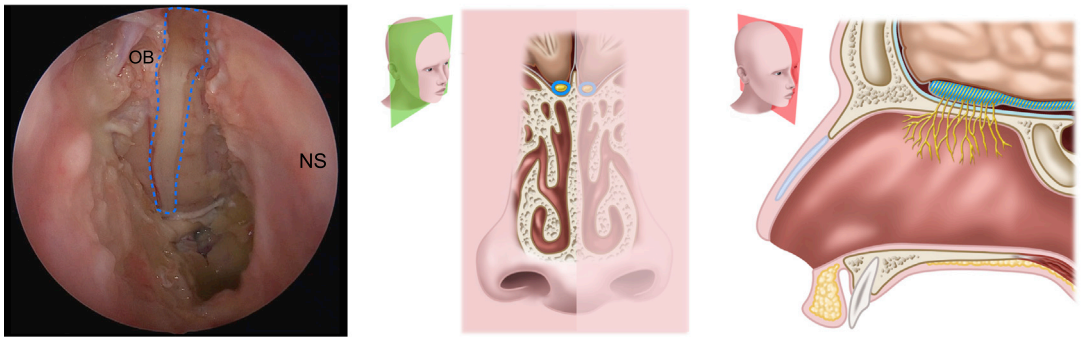

Figure 1. Postmortem bedside surgical procedure for tissue sample harvesting

(A) Immediately after the death of a hospitalized COVID-19 patient or a control patient, the ENT team was contacted by phone, and they harvested samples bedside using an adapted endoscopic endonasal transcribriform approach.

(B) Cohort of 68 COVID-19 patients. Time variables are expressed as median and interquartile range Q1–Q3. All other variables are expressed as percentages.

(legend continued on next page)

sense of smell (Lechien et al., 2021; Vaira et al., 2021; Whitcroft and Hummel, 2020; Xydakis et al., 2020, 2021). An unresolved question is whether the olfactory nerve can provide SARS-CoV-2 with a route of entry to the brain (Butowt et al., 2021).

Soon after SARS-CoV-2 made its entry on the scene, the expression patterns of the virus cell entry genes *ACE2* and *TMPRSS2* were characterized in the human and mouse olfactory system (Brann et al., 2020; Fodoulian et al., 2020). The inference was drawn that sustentacular cells but not olfactory sensory neurons (OSNs) might be the susceptible cell type in the olfactory epithelium (OE) (Cooper et al., 2020). But, puzzlingly, two of the other six human coronaviruses, SARS-CoV (Fung and Liu, 2019) and the endemic HCoV-NL63 (Hofmann et al., 2005; van der Hoek et al., 2004), also use ACE2 for cell entry but do not commonly cause olfactory dysfunction (Zugaj et al., 2021). SARS-CoV-2 replication in sustentacular cells of COVID-19 patients remains to be demonstrated.

Historically, histological and molecular studies of normal and diseased human olfactory mucosa (OM) and olfactory bulb (OB) have been few and far between. Harvesting samples of suitable quality and unambiguous identity has proved problematic, both from living and deceased patients. Macroscopically the OM cannot be distinguished from the respiratory mucosa (RM). Anatomically the OM is made up of an archipelago of islands of various sizes scattered amidst RM high up in the nasal cavity within the olfactory cleft (Engström and Bloom, 1953; Escada, 2013; Kachramanoglou et al., 2013; Kern, 2000; Naessen, 1970; Pinna et al., 2013; Salazar et al., 2019). In contrast to the OM in laboratory rodents, the human OM is not a uniform sensory sheet (Morrison and Costanzo, 1990, 1992). Patches of aneuronal epithelium are intercalated with patches containing abundant OSNs in human OE (Holbrook et al., 2005, 2011; Tanos et al., 2017). The OM consists of OE and lamina propria (LP), and these two layers are bound tightly together by a basal lamina. Simply put, it is not possible to collect samples of pure human OM, let alone of pure human OE. Furthermore, OB biopsies cannot be taken from living patients due to the intracranial position and debilitating consequences of the intervention. Harvesting OM and OB in the conventional setting of an autopsy is often feasible only after a long postmortem interval (PMI), particularly in COVID-19 patients who may still be contagious (Gagliardi et al., 2021; Matschke et al., 2020). Analysis of samples procured after long PMIs is clouded by limitations resulting from autolysis of cells and tissues (Meinhardt et al., 2021).

We reasoned that, to achieve a drastic reduction of the PMI, tissue harvesting best be performed bedside, soon after death. We further reasoned that, to investigate how the sequence of pathobiological events leading to olfactory dysfunction is initiated, the study design must accommodate the inclusion of patients in an acute phase of the infection, enabling us to catch the virus as it strikes.

Here, we have developed a postmortem bedside surgical procedure, which we adapted from an endoscopic technique of skull base surgery, to harvest RM and OM tissue samples and whole OBs. We visualized how SARS-CoV-2 attacks the olfactory system by combining the RNAscope platform of ultrasensitive single-molecule fluorescence *in situ* RNA hybridization with fluorescence immunohistochemistry (IHC). We identified ciliated cells in the RM and sustentacular cells in the OM as the major target cell types for SARS-CoV-2 replication in the nasal mucosa. A subset of cases showed viral RNA in the leptomeningeal layers surrounding the OB, but invariably the OB parenchyma was spared from infection. The absence of evidence for infection of OSNs and of OB neurons suggests that SARS-CoV-2 is not a neurotropic virus. We postulate that infected sustentacular cells transiently provide insufficient support to OSNs, structural and/or physiological.

RESULTS

Postmortem bedside surgical procedure

We designed a 24/7 workflow initiated by a health care worker of an intensive care unit (ICU) or a ward placing a phone call to a team of ear, nose, and throat (ENT) physicians shortly after the death of a COVID-19 patient (Figure 1A). The ENT team wore personal protective equipment (Van Gerven et al., 2020) and performed an endoscopic surgical procedure at the bed of the deceased patient with a preassembled mobile unit consisting of a monitor, light source, camera, and endoscopic equipment. This concept was the foundation of a clinical study called ANOSMIC-19, ANalyzing Olfactory dySfunction Mechanisms In COVID-19. We included a cohort of 68 patients who died from or with COVID-19 in the University Hospitals Leuven (Leuven, Belgium) or in the General Hospital Sint-Jan Brugge-Oostende AV (Bruges, Belgium) between May 2020 and April 2021 (Figure 1B). In parallel we included 15 control patients and two convalescent COVID-19 patients who died in a hospital several months after recovering (Figure S1). Our cohort of COVID-19 cases is representative of the rather uniform phenotype of deceased COVID-19 patients (Patel et al., 2021; Van Aerde et al., 2020): predominantly men suffering from multiple comorbidities, most commonly obesity or overweight, diabetes mellitus type 2, and hypertension.

We adapted the postmortem bedside surgical procedure from the endoscopic endonasal transcribriform approach in skull base surgery (Kassam et al., 2005) (Video S1). Briefly, to harvest samples of the RM, we resected separately the inferior, middle, and often also the superior turbinates of the nasal cavity with Heymann nasal scissors (Figure 1C). Next, to harvest samples of the OM, we dissected the lining of the olfactory cleft including the superior part of the septum and the cribriform plate with a sickle knife, while transecting the fila olfactoria (Figure 1D). Subsequently, we removed the bony part of the anterior skull base

(C–E) Endoscopic images (left) taken prior to harvesting samples of RM (C) and OM (D), and whole OBs (E). Illustrations indicate the location of the resected tissue (marked in blue) on a coronal section (middle) and a parasagittal (C) or midsagittal (D and E) section (right). Frozen frames were collected from the video of the procedure performed in the right nasal cavity of COVID #33 with a 4 mm 0° endoscope.
IT, inferior turbinate; MT, middle turbinate; NS, nasal septum; OC, olfactory cleft. The 3D head models show the corresponding planes. See also Figures S1, S3, and S4.

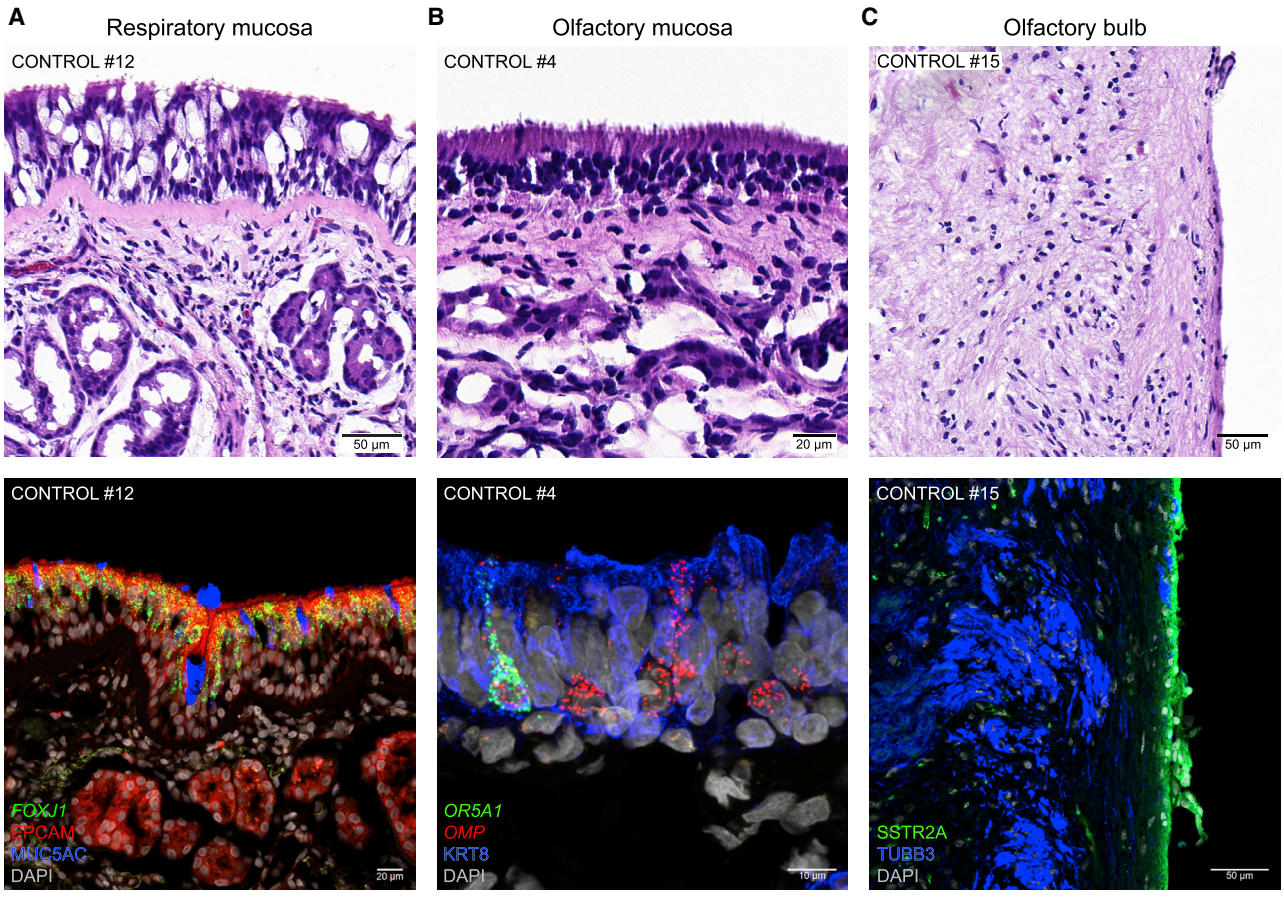

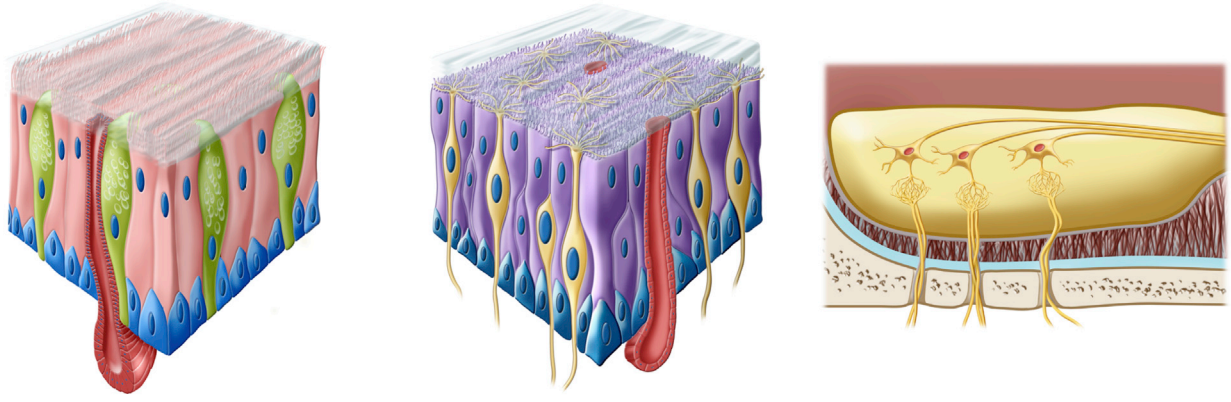

Cell type	Marker
Ciliated cell	*FOXJ1*, EPCAM, KRT7, KRT8
Goblet cell	MUC5AC
Duct cell	EPCAM, KRT8, MUC5AC
Basal cell	KRT5/6

Cell type	Marker
Sustentacular cell	*UGT2A1, GPX3, SOX2,* ERMN, KRT8, KRT18
Olfactory sensory neuron	*OMP, ANO2, CNGA2, GNAL, OR*, TUBB3
Duct cell	*UGT2A1, GPX3*, KRT8, KRT18
Basal cell	KRT5/6

Cell type	Marker
Axon of olfactory sensory neuron	TUBB3
Leptomeninges	SSTR2A

Figure 2. Respiratory mucosa, olfactory mucosa, and olfactory bulb in control patients

Brightfield images of hematoxylin and eosin-stained sections (top), confocal images of sections stained fluorescently with RNAscope and IHC (middle), and schematics of the main cell types with the genes (italics) and proteins (roman) used as markers (bottom).

(A) RM of control #12. *FOXJ1* is a marker for ciliated cells and EPCAM for epithelial cells. The MUC5AC-IR signal labels goblet cells and identifies blobs of secreted mucus.

(legend continued on next page)

with a hammer and chisel instead of a drill, avoiding aerosol formation in these patients, some of whom might still have been contagious. After making a longitudinal incision of the dura mater, we detached the OB from the overlying part of the brain using a ball probe, ensuring atraumatic removal of the tissue, and transected the OB from the olfactory tract as posteriorly as possible (Figure 1E). We performed the procedure on the left and right nasal cavity, and the identical procedure on control patients.

In summary, we drastically reduced the PMI: the median was 67 minutes for COVID-19 ICU patients, 85 for COVID-19 ward patients, and 89 for control patients.

Combining ultrasensitive *in situ* RNA hybridization with immunohistochemistry

We reasoned that visualizing the target cell types of an RNA virus ought to be conducted first and foremost by RNA *in situ* hybridization. We opted for the RNAscope technology, which visualizes a single RNA molecule as a dot or "punctum," plural "puncta" (Wang et al., 2012). Fluorescence RNAscope can be combined with fluorescence IHC, which visualizes an antigen as an immunoreactive (IR) signal. Often the IR signal diffusely fills a cell and consequently outlines its contours, facilitating cell-type identification.

Figure 2 shows images of cryosections of RM, OM, and OB in control patients. We identified cell types by a combination of their expression of markers for RNA (names in italics) and proteins (names in roman), their morphology, and their position within the tissue.

The RM lines the majority of the inner surface of the nasal cavity (Figure 2A). The pseudostratified respiratory epithelium (RE) is delineated from the LP by a thick basal lamina. Main cell types of the RE include ciliated cells, goblet cells, and basal cells. *FOXJ1*, which encodes a transcription factor involved in ciliogenesis, is a marker for ciliated cells, whose cilia continuously sweep the overlying mucus to the nasopharynx. EPCAM, a cell-adhesion molecule, labels ciliated cells in the RE and cells of mucus-producing glands and their ducts in the LP. The mucin MUC5AC, a gel-forming glycoprotein protecting the RM, is a marker for goblet cells, and the MUC5AC-IR signal also identifies secreted blobs of mucus.

The OM is a minor constituent of the nasal mucosa (Figure 2B). Main cell types of the pseudostratified OE are OSNs at various stages of maturation, non-neuronal sustentacular or supporting cells, and basal cells, which are stem cells that regenerate OSNs and sustentacular cells throughout the life of the individual. Apically, mature OSNs sprout cilia and sustentacular cells sport microvilli. Sustentacular cells can be identified by several markers including cytokeratin KRT8, and their morphology and position in the OE are characteristic: they span the apical-basal width of the OE, apically they form a layer devoid of nuclei, and basally they taper off and extend foot processes onto a thin basal lamina, which delineates the OE from the LP. A classic marker for mature OSNs is olfactory marker protein (OMP). A mature OSN is thought to express only one intact odorant receptor (OR) gene (Buck and Axel, 1991) out of a repertoire of 389 genes (Barnes et al., 2020). An OSN is shown harboring puncta for *OR5A1*, the major receptor for β-ionone, a key aroma in food and beverages (Jaeger et al., 2013). Puncta for an OR gene assume a characteristic pattern resembling the shape of a cherry.

The OB resides within the cranial cavity (Figure 2C). It receives ipsilateral input from fila olfactoria, bundles of OSN axons that course through a few dozen holes in the sieve-like cribriform plate (Favre et al., 1995; López-Elizalde et al., 2018; Vasvári et al., 2005). TUBB3, a component of microtubules, is a classic marker of neurons and axons (Lee et al., 1990; Zapiec et al., 2017). TUBB3-IR OSN axons coalesce into glomeruli in the OB. The surface of the OB is covered snugly with pia mater, a thin leptomeningeal layer that is IR for SSTR2A, somatostatin receptor 2 (Boulagnon-Rombi et al., 2017; Menke et al., 2015). The other leptomeningeal layer is the arachnoid, a spider web-like structure that connects to the dura mater, the tough outer meningeal layer close to the skull. Cerebrospinal fluid circulates continuously between the pia mater and the arachnoid.

In summary, our rapid approach of tissue sample procurement allowed us to generate, from 100% of cases, high-quality confocal images combining RNAscope with IHC.

Viral RNAscope probes and antibody

SARS-CoV-2 is a positive-sense single-strand RNA virus. A negative-sense full-length replicative intermediate and multiple negative-sense subgenomic RNAs are produced during the viral life cycle (Brant et al., 2021; Kim et al., 2020; Sola et al., 2015; V'kovski et al., 2021). Negative-sense RNAs reflect ongoing viral replication and are not present in virions.

We used a panel of seven RNAscope probes: *SARS-CoV-2-N* (nucleocapsid, giving rise to puncta hereafter abbreviated as *N* puncta), *SARS-CoV-2-S* (spike; *S* puncta), *SARS-CoV-2-M* (membrane; *M* puncta), *SARS-CoV-2-orf1ab* (open reading frames 1a and 1b; *orf1ab* puncta), *SARS-CoV-2-N-sense* (*N-sense* puncta), *SARS-CoV-2-S-sense* (*S-sense* puncta), and *SARS-CoV-2-orf1ab-sense* (*orf1ab-sense* puncta). The *sense* probes detect negative-sense RNAs, with puncta occurring perinuclearly (Chandrashekar et al., 2020; Liu et al., 2020). We also did IHC with an antibody against nucleocapsid. Figure S2 shows negative controls for the probes and the antibody.

SARS-CoV-2 infects ciliated cells in the respiratory epithelium

To provide suitable context for the examination of the samples of olfactory cleft mucosa, we first examined the RM samples (Figure 3).

We detected viral presence in the RM of 30 of the 68 (44%) COVID-19 cases. Henceforth, we refer to this subset as the

(B) OM of control #4. *OR5A1* is one of the 389 OR genes in the human genome. *OMP* is a marker for mature OSNs, and KRT8 for sustentacular cells.
(C) OB of control #15. SSTR2A is a leptomeningeal marker, and TUBB3 a neuronal and axonal marker. In the schematic, the pia mater is depicted as a thin gray line surrounding the OB, the dura mater as a thick light-blue line, and the arachnoid as a brown spider web-like structure between the pia mater and the dura mater. Axons of OSNs course through holes of the cribriform plate and synapse with three second-order neurons in the OB. DAPI served as nuclear stain. The schematics show the main cell types that we studied.

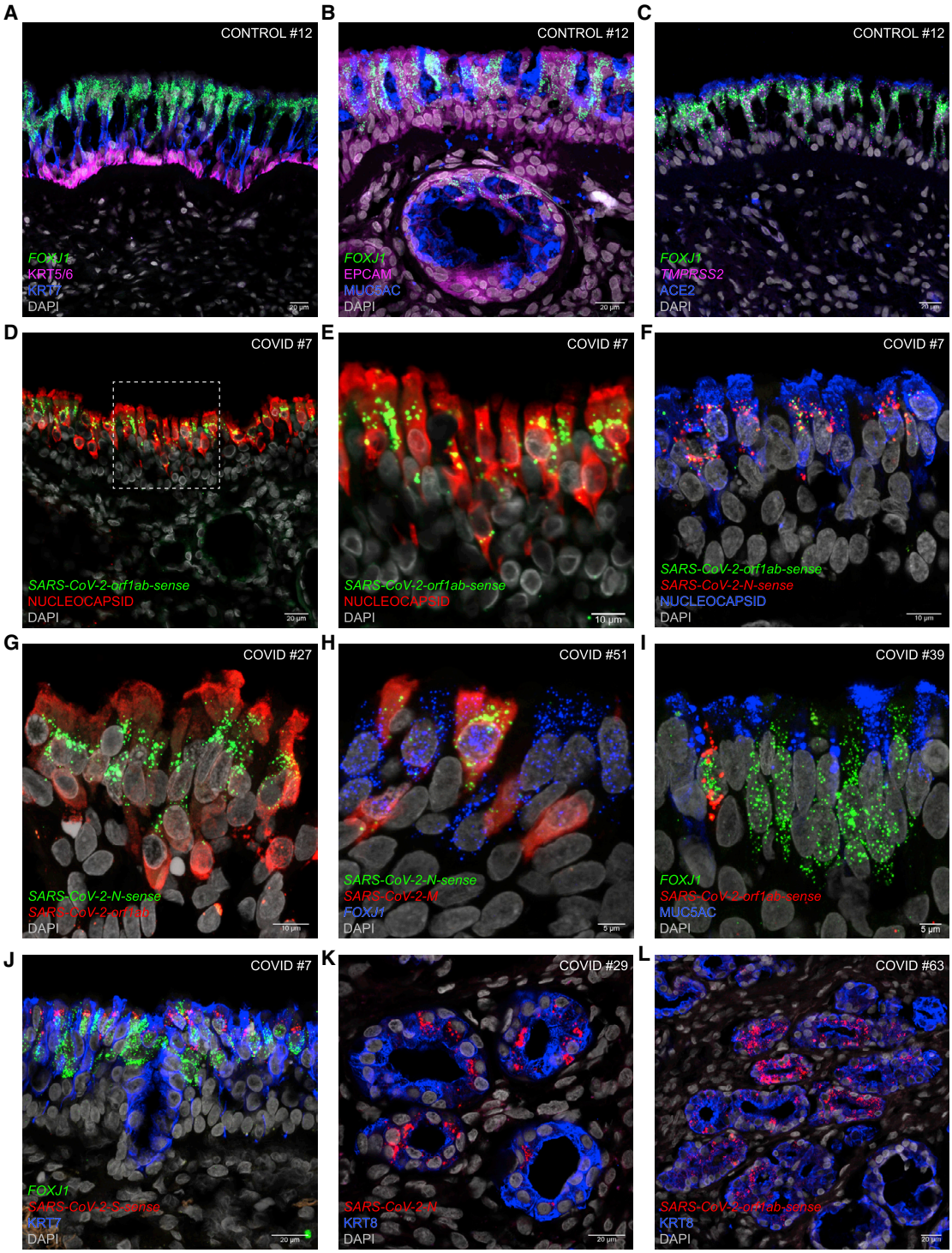

Figure 3. Infection of the respiratory mucosa by SARS-CoV-2

(A–C) Confocal images of sections through the RM of control #12. *FOXJ1* and KRT7 are markers for ciliated cells, and KRT5/6 for basal cells (A). EPCAM is a marker for epithelial cells in the RE and the LP, MUC5AC for goblet cells in the RE, and cells lining a transversely cut gland duct in the LP (B). The ACE2-IR signal caps the surface of the RE, and *TMPRSS2* puncta cluster with *FOXJ1* puncta in ciliated cells (C).

(D–L) Confocal images of sections through the RM of COVID #7, #27, #51, #39, #29, and #63. Widespread nucleocapsid-IR signal occurs apically within the RE, and *orf1ab-sense* puncta reflect ongoing viral replication (D). The dashed square in (D) is the area magnified in (E). *N-sense* puncta cluster with *orf1ab-sense*

(legend continued on next page)

"informative" cases. They died within 16 days after diagnosis of COVID-19 by reverse-transcription quantitative polymerase chain reaction (henceforth abbreviated as PCR), except for COVID #29, the immunosuppressed recipient of a solid organ transplant who died 29 days after diagnosis (Figure S3). We did not detect *SARS-CoV-2* puncta in the RM, OM, or OB of the other 38 ("non-informative") COVID-19 cases, of the two convalescent COVID-19 cases, and of the 15 control cases. For COVID #9 through #70, we carried out rapid antigen tests on nasopharyngeal (NP) swabs that we took endoscopically prior to the procedure (Video S1 at 0'31") and found a high concordance with the RNAscope data (Figure S4A). For 11 COVID-19 cases, we obtained PCR data on a second NP swab that we took preprocedurally (Figure S4B).

We identified ciliated cells as the major target cell type for SARS-CoV-2 in the RM of 27 of the 30 (90%) informative cases and cells lining gland ducts in the LP in 4 (13%).

Figures 3A–3C show confocal images of sections of the RM of control case #12. Ciliated cells are diffusely filled with KRT7-IR signal and harbor *FOXJ1* puncta, whereas IR signal for cytokeratins KRT5/6 labels a basal layer of cells delineating the RE from the LP (Figure 3A). EPCAM-IR signal labels epithelial cells, and MUC5AC-IR signal labels mucin-producing cells and identifies blobs of mucus (Figure 3B). The ACE2-IR signal forms a discontinuous thin band at the luminal surface of the RE and puncta for *TMPRSS2* abound throughout the RE (Figure 3C).

In the RE of COVID #7, nucleocapsid-IR signal diffusely fills an uninterrupted apical row of cells (Figures 3D and 3E). The timeline of infection is exceptionally well defined for this patient, who died 78 h after diagnosis, which was preceded by two negative PCR results from NP swabs taken 3 and 6 days earlier. Consistent with the acute phase of the infection, nucleocapsid-IR cells harbor perinuclear *orf1ab-sense* puncta. Perinuclear *N-sense* puncta cluster with *orf1ab-sense* puncta in nucleocapsid-IR cells in COVID #7 (Figure 3F) and with densely packed *orf1ab* puncta in COVID #27 (Figure 3G). In COVID #51, perinuclear *N-sense* puncta cluster with *M* and *FOXJ1* puncta (Figure 3H). In COVID #39, perinuclear *orf1ab-sense* puncta cluster with *FOXJ1* puncta within an individual ciliated cell (Figure 3I). Perinuclear *S-sense* puncta cluster with *FOXJ1* puncta in KRT7-IR cells in COVID #7 (Figure 3J).

In 4 of the 30 informative cases, cells lining gland ducts in the LP were infected. In COVID #29, #63, and #67, only the ducts were infected, and in COVID #60 both the RE and the ducts were infected. KRT8-IR cells lining gland ducts in the LP harbor densely packed *N* puncta in COVID #29 (Figure 3K) and *orf1ab-sense* puncta in COVID #63 (Figure 3L). Initially, COVID #63 was included as a control case, with a negative PCR result from a NP swab taken 82 h prior to the time of death but tested PCR positive on a swab that we took postmortem. COVID #63 has the shortest period between diagnosis and death in our cohort.

In summary, the RM is a major site of infection for SARS-CoV-2 and represents a vast area of cells susceptible to virus entry and replication (Wölfel et al., 2020; Zou et al., 2020). Ciliated cells are the major target cell type in the RE, and, in a subset of patients, cells lining gland ducts in the LP are infected.

Post hoc scoring of infection with B.1.1.7/Alpha versus non-B.1.1.7/non-Alpha

In late 2020, variant of concern B.1.1.7 made its entry into the SARS-CoV-2 landscape in Belgium and rapidly took over to become the dominant lineage during the third wave of the COVID-19 pandemic in Belgium. Later known as the Alpha variant, B.1.1.7 is characterized by a higher transmissibility (Davies et al., 2021) and higher viral load (Jones et al., 2021). A 6-nucleotide deletion in *S* encoding the amino acids HV is specific for the Alpha variant, and a 9-nucleotide deletion in *orf1ab* encoding SGF of the non-structural protein nsp6 is present in the Alpha, Beta, and Gamma variants (Martin et al., 2021; Peacock et al., 2021). We designed a chromogenic assay with custom probes for BaseScope, a version of the RNAscope platform specific for subtle mutations.

We obtained variant of concern-specific PCR or sequence data for 35 COVID-19 cases, among whom are COVID #60 (infected with a non-Alpha lineage) and COVID #68 (infected with Alpha). In the RE of COVID #60 (a patient with an active oncological condition who died 40 h after diagnosis), a fraction of cells harboring *FOXJ1* puncta are diffusely filled with nucleocapsid-IR signal, and most of these cells harbor perinuclear *orf1ab-sense* puncta (Figure 4A, top). In the RE of COVID #68 (a patient with an active oncological condition who died 5 days after diagnosis), perinuclear *S-sense* puncta cluster with *FOXJ1* puncta in nucleocapsid-IR cells (Figure 4A, bottom). A mix of two BaseScope probes for the wild-type or deletion form of *S* yielded either a teal or red precipitate in the RE of COVID #60 or of COVID #68, respectively (Figure 4B). A mix of two BaseScope probes for the wild-type or deletion form of *orf1ab* supported this binary genotyping (Figure 4C).

In summary, we have developed a post hoc assay for differential diagnosis of infection with Alpha versus non-Alpha lineages in fixed tissue samples.

SARS-CoV-2 infects sustentacular cells in the olfactory epithelium

Next, we analyzed samples from olfactory cleft mucosa (Figures 5 and S5). We faced the challenge that islands of OM are scattered among RM and comprise areas of OE in which OSNs are sparse or even absent. We rigorously defined "OM" by the expression of neuronal markers including puncta for *ANO2*, *CNGA2*, *GNAL*, *GNG13*, *OMP*, and OR genes and TUBB3-IR signal. We detected *SARS-CoV-2* puncta and nucleocapsid-IR signal in the OM of 6 of the 30 (20%) informative cases. We identified sustentacular cells as the major target cell type in the OE and failed to find evidence for infection of OSNs.

Figures 5A and 5B show the OM of control case #4. Sustentacular cells are diffusely filled with KRT8-IR signal and harbor

puncta in nucleocapsid-IR cells (F) and with *orf1ab* puncta (G). Ciliated cells harbor *N-sense*, *M*, and *FOXJ1* puncta (H). An individual ciliated cell harbors *orf1ab-sense* and *FOXJ1* puncta (I). Ciliated cells harbor *S-sense* and *FOXJ1* puncta and contain KRT7-IR signal (J). KRT8-IR cells lining gland ducts in the LP harbor *N* puncta (K) or *orf1ab-sense* puncta (L). DAPI served as nuclear stain.
See also Figure S2.

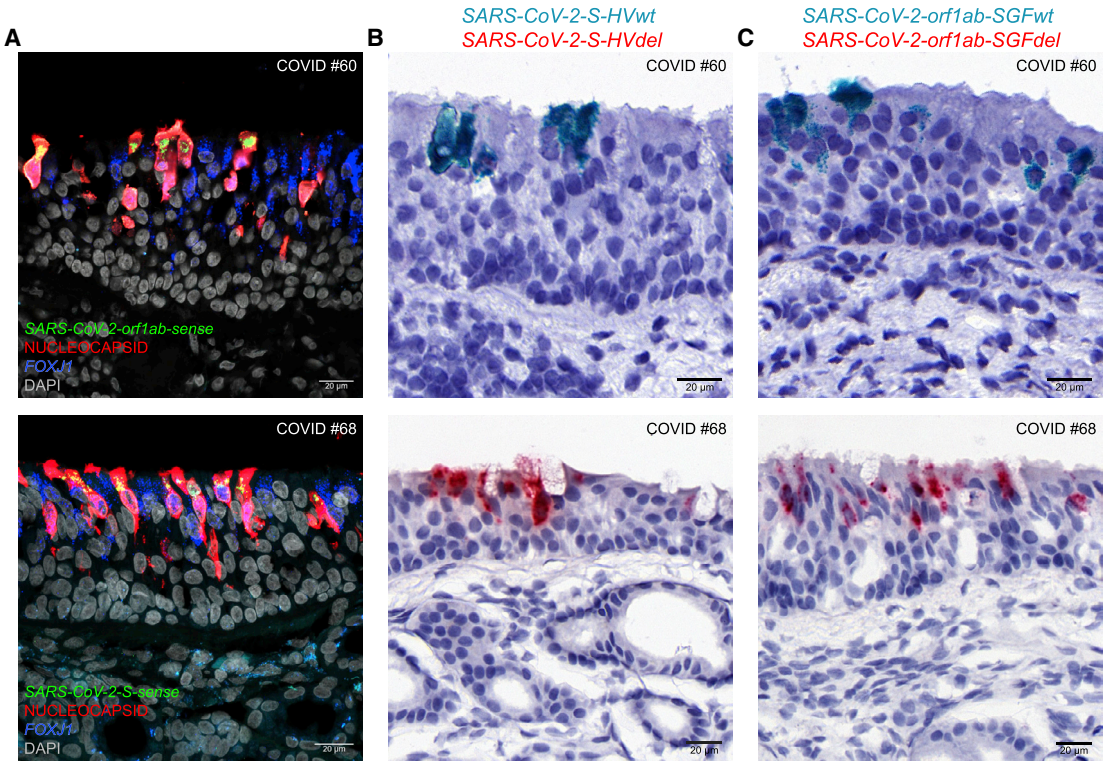

Figure 4. Infection of the respiratory mucosa with B.1.1.7/Alpha versus non-B.1.1.7/non-Alpha

(A) Confocal fluorescence images of sections through the RM of COVID #60, infected with a non-Alpha lineage (top), and of COVID #68, infected with Alpha (bottom). Several ciliated cells harboring *FOXJ1* puncta are diffusely filled with nucleocapsid-IR signal, and some contain *orf1ab-sense* puncta (top) or *S-sense* puncta (bottom). DAPI served as nuclear stain.

(B and C) BaseScope chromogenic stainings with a mix of two probes designed for wt *S* and the HV deletion (B), or a mix of two probes designed for wt *orf1ab* and the SGF deletion (C). The presence of teal and absence of red precipitate is diagnostic for infection with a non-Alpha lineage (B and C, top). Conversely, the presence of red and absence of teal precipitate is consistent with infection with Alpha (B and C, bottom).

TMPRSS2 puncta, and four adjacent OSNs harbor puncta for a pool of probes for OR genes *OR5A1*, *OR5AN1*, *OR7C1*, and *OR11A1* (Figure 5A). ACE2-IR crest-like stripes cap an array of intertwined KRT8-IR sustentacular cells and TUBB3-IR OSNs (Figure 5B). An image of COVID #22, who died 26 days after diagnosis and had no detectable *SARS-CoV-2* puncta in any tissue sample, showcases the three major cell types of the OE (Figure 5C). Puncta for *GPX3*, which encodes a glutathione peroxidase, label sustentacular cells from apical to basal and Bowman's gland cells in the LP. Puncta for *ANO2*, which encodes the chloride channel in the olfactory signal transduction pathway, label the middle layer of OSNs. The KRT5/6-IR signal labels the basal layer of cells.

A highly informative case is COVID #8, who died 4 days after diagnosis. TUBB3-IR cells (OSNs) do not contain nucleocapsid-IR signal, and sustentacular cells harbor *UGT2A1* puncta (Figure 5D). *N* puncta diffusely fill a great many sustentacular cells spanning the width of the OE from apical to basal; interestingly, the KRT8-IR signal identifies a patch of uninfected sustentacular cells, whereas infected sustentacular cells are low on or negative for KRT8-IR signal (Figure S5A). *N* puncta are densely packed in cells with the typical shape of sustentacular cells (resembling a wine glass with a twisted stalk touching the basal lamina), and the wider apical parts of infected sustentacular cells are intermingled with those of uninfected sustentacular cells harboring *UGT2A1* puncta and capped with IR signal for ERMN, a sustentacular cell marker (Figures 5E and S5B). That infected sustentacular cells are low on or negative for puncta or IR signal for a given marker is consistent with SARS-CoV-2-elicited decay of host mRNAs and inhibition of host protein translation (Banerjee et al., 2020; Burke et al., 2021; Finkel et al., 2021; Schubert et al., 2020; Zhang et al., 2021). This multipronged viral takeover is illustrated by a single infected sustentacular cell standing out among uninfected sustentacular cells (Figure 5F): this cell is devoid of *GPX3* puncta, is filled diffusely with nucleocapsid-IR signal from apical to basal, and harbors perinuclear *orf1ab-sense* puncta.

We exhaustively searched for the presence of *sense* puncta and nucleocapsid-IR signal in OSNs but failed to find it. By way of example of the negative evidence, *S-sense* puncta occur in the apical layer along with KRT8-IR signal, whereas puncta for the pool of four OR gene probes occur in the middle layer (Figure 5G). A high-magnification image shows that OSNs harboring puncta for the probe pool do not harbor perinuclear *S-sense* puncta (Figure 5H). The apical layer harboring *S-sense* puncta and containing KRT8-IR signal is mutually exclusive with the

middle layer of OSNs harboring puncta for the probe pool (Figure 5I). An individual OSN harboring puncta for the OR gene *OR7C1* as well as several TUBB3-IR cells surrounding it do not harbor *S-sense* puncta (Figure 5J).

We confirmed these observations in another case, COVID #7. We identified OSNs with *CNGA2* puncta and TUBB3-IR signal (Figures S5C and S5D) or *GNAL* puncta (Figure S5E). Among several uninfected sustentacular cells harboring puncta for *SOX2* (Durante et al., 2020), two cells harbor perinuclear *orf1ab-sense* puncta (Figure S5F). Sustentacular cells harboring densely packed *N* puncta stand out by the depletion of the KRT18-IR signal (Figures S5G and S5H). In COVID #57 (Figure S5I) and COVID #25 (Figure S5J), the infected OE is damaged, with swaths of tissue sloughing off; it may well be at the verge of desquamation.

In summary, sustentacular cells are the major target cell type in the olfactory mucosa. We failed to find evidence for infection of OSNs. The pattern of infection of the OM is patchy.

Spatial whole-transcriptome profiling of the olfactory epithelium of COVID #8

Could infection of sustentacular cells have an indirect effect on OR gene expression in OSNs during the acute phase of the infection? To address this hypothesis, we leveraged GeoMx Digital Spatial Profiling (Beechem, 2020; Merritt et al., 2020) with the Whole Transcriptome Atlas (WTA) for 18,318 human transcripts (Delorey et al., 2021; Jerby-Arnon et al., 2021).

COVID #8 was best suited for this analysis due to the abundance of mature OSNs, the contiguous stretches of OE several millimeters in length, and the geometric specifics of the patchiness of the infection. We analyzed one slide with six adjacent sections of the OM of COVID #8 (Figure 6), which were adjacent to the sections shown in Figure 5. The slide was stained fluorescently with an RNAscope probe for *S* and IHC for KRT8/18 and pan-KRT. The slide was then hybridized with WTA probes and spike-ins for *orf1ab* and *S*. Guided visually by the intensity of the fluorescent signal from the *S* puncta, we selected 17 areas of interest (AOI) within the OE: 10 with high viral load (ORF1ab High) and 7 with low viral load (ORF1ab Low) (Figure 6A). Two AOIs are shown in magnification: AOI 13 contains 414 nuclei within an area of 25,741 μm^2, and AOI 7 contains 420 nuclei within 38,994 μm^2 (Figure 6B). There is no significant difference in nucleus counts between the two types of AOIs (Figure 6C). Each AOI was UV-illuminated individually to photocleave the WTA probes for collection and sequencing. The normalized expression counts for *orf1ab* in ORF1ab High versus ORF1ab Low AOIs fit well with our visual judgment of the confocal scans (Figure 6D). The *S* and *orf1ab* counts have a Pearson's correlation coefficient of 0.998 (Figure 6E). Differential expression modeling of 9,262 genes detected in at least 20% of the AOIs reveals that in ORF1ab High AOIs, the normalized expression counts for sustentacular cell markers *GPX3*, *KRT8*, and *KRT18* are significantly reduced and those for OSN markers *ANO2* and *GNG13* are significantly increased (Figure 6F). When including marker genes enriched in ORF1ab High AOIs but with larger p values, the averages of the $\log_2$ fold change (FC) for eight sustentacular cell markers (−0.80, SD = 0.30) and eight OSN cell markers (0.69, SD = 0.26) are of the same magnitude but in opposing directions (Figure 6G). After flipping the sign of the FCs for sustentacular cell markers, the null hypothesis that there is no difference in magnitude with the FCs for OSN markers was not rejected (t test: $t = -0.84$, $df = 13.7$, $p < 0.4154$). In other words, the FC values for the two major cell types of the AOIs are anti-correlated. The average of the $\log_2$ FC for the 26 OR genes detected (0.66, SD = 0.64) does not differ significantly from that of the eight OSN cell markers (t test: $t = -0.14$, $df = 29.321$, $p < 0.89$) (Figure 6H). Reassuringly, the four OR genes *OR5A1*, *OR5AN1*, *OR7C1*, and *OR11A1* for which we had identified numerous cells in adjacent sections by RNAscope in Figure 5 were among the 26 OR genes detected by WTA profiling.

In summary, the intra-slide approach of spatial whole-transcriptome profiling revealed no changes in OR gene-expression levels in OE patches of high versus low viral load in COVID #8.

SARS-CoV-2 can make it to the leptomeningeal layers surrounding the olfactory bulb but spares its parenchyma

Consistent with the absence of evidence for infection of OSNs, we failed to find evidence for viral invasion of the OB parenchyma. Surprisingly, we discovered viral RNA within the leptomeningeal layers surrounding the OB in 11 of the 30 (37%) informative cases (Figure 7).

In COVID #16 (a patient with an active oncological condition who died 8.5 days after diagnosis), a tiled confocal image of a sagittal section of a whole OB shows SSTR2A-IR signal labeling the pia mater and the arachnoid, and TUBB3-IR signal labeling incoming OSN axons and OB neurons (Figure 7A). A high-magnification image shows *N* puncta at the side of the pia mater abutting the OB (Figure 7B). In an adjacent section of the same OB, densely packed *N* puncta occur within a segment of the pia mater together with the abundant nucleocapsid-IR signal, a combination that may reflect free virions, but not in the OB parenchyma (Figure 7C). In another section, *S* puncta occur within an obliquely cut blood vessel defined by *PECAM1* puncta in endothelial cells (Figure 7D). In COVID #7, *N* puncta occur in a swath of SSTR2A-IR pia mater that is partially detached, but not in the OB parenchyma (Figure 7E). In COVID #27 (who died 93 h after diagnosis), densely packed *M* puncta occur in the pia mater covering the OB and outside the confines of a blood vessel harboring *PECAM1* puncta but not in the OB parenchyma (Figure 7F). In COVID #60 (a patient with an active oncological condition who died 40 h after diagnosis), a leptomeningeal sample near the OB that includes the transition zone to the dura mater contains abundant *N* and *S* puncta scattered among the SSTR2A-IR signal (Figure 7G).

In summary, SARS-CoV-2 does not appear to be a neurotropic virus, in the sense that it does not infect OSNs and OB neurons.

DISCUSSION

We have here taken a virocentric view of COVID-19, from the viewpoint of SARS-CoV-2 acutely attacking the human olfactory system. We identified sustentacular cells as the main target cell type in the OM, failed to find evidence for infection of OSNs and of the OB parenchyma, and discovered viral RNA in the leptomeningeal layers surrounding the OB.

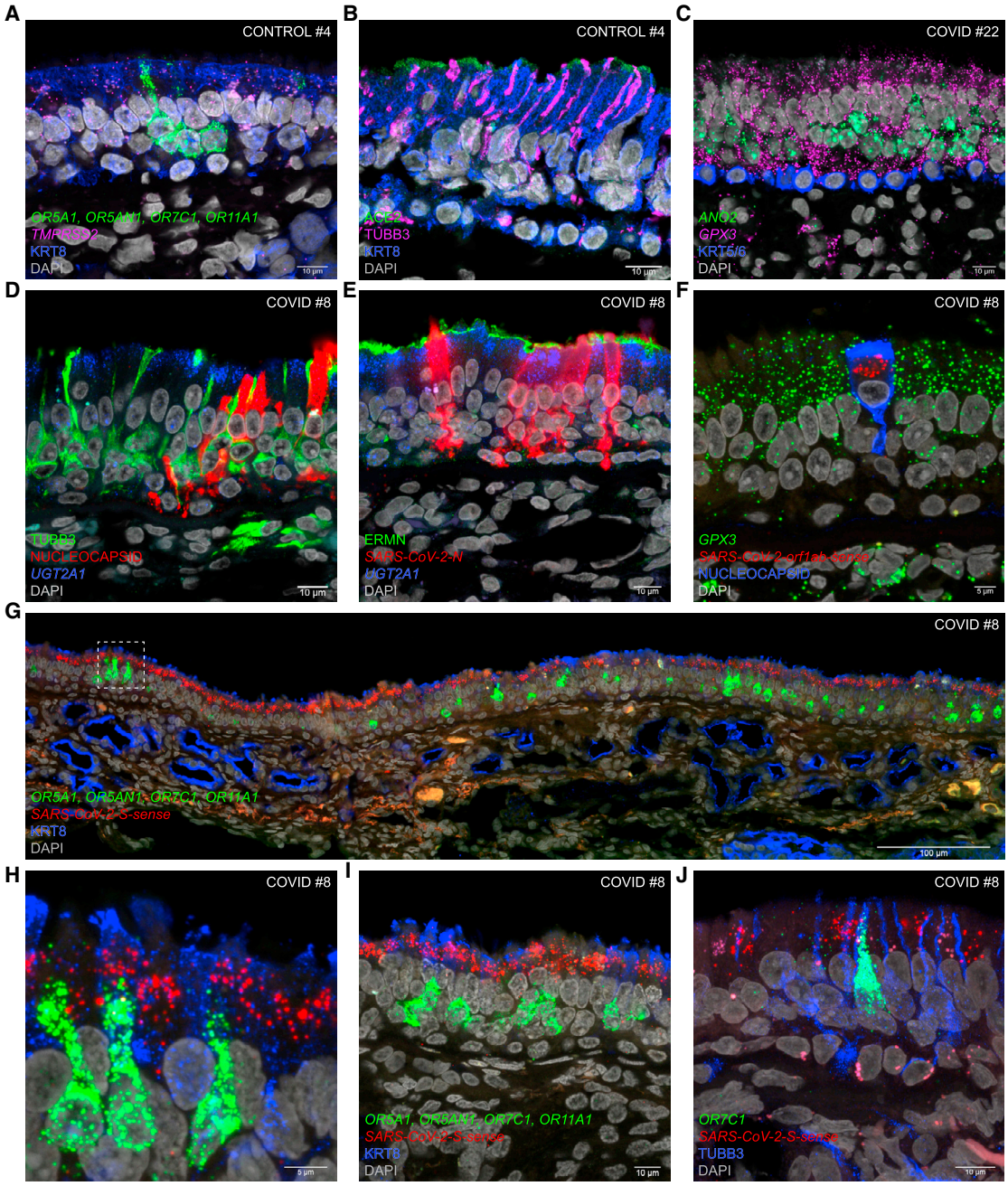

Figure 5. Infection of the olfactory mucosa by SARS-CoV-2

(A–C) Confocal images of sections through the OM of control #4 (A and B) and non-infected OM of COVID #22 (C). Four OSNs harbor puncta for a pool of probes for four OR genes, and KRT8-IR sustentacular cells harbor *TMPRSS2* puncta (A). ACE2-IR crests face the lumen of the nasal cavity (B). *ANO2* is a marker for mature OSNs, *GPX3* for sustentacular cells, and KRT5/6 for basal cells (C).

(D–J) Confocal images of sections through the OM of COVID #8. Nucleocapsid-IR signal occurs in a few sustentacular cells but not in TUBB3-IR OSNs, and uninfected sustentacular cells harbor puncta for *UGT2A1*, a gene encoding an UDP glucuronosyltransferase (D). *N* puncta are densely packed in several sustentacular cells, which are low on or devoid of *UGT2A1* puncta and ERMN-IR signal, whereas uninfected sustentacular cells harbor *UGT2A1* puncta and are capped with ERMN-IR signal (E). Uninfected sustentacular cells harbor *GPX3* puncta but not an individual sustentacular cell diffusely filled with nucleocapsid-IR signal and harboring *orf1ab-sense* puncta (F). Numerous OSNs in the middle layer harbor puncta for the probe pool, and the apical layer of KRT8-IR sustentacular cells harbors *S-sense* puncta (G and H). The dashed square in (G) is the area magnified in (H). *S-sense* puncta occur in the apical layer of KRT8-IR sustentacular cells, but not in OSNs harboring puncta for the probe pool (I) and not in an individual *OR7C1*$^{+}$ OSN and in surrounding TUBB3-IR cells (J).

DAPI served as nuclear stain. See also Figures S2 and S5.

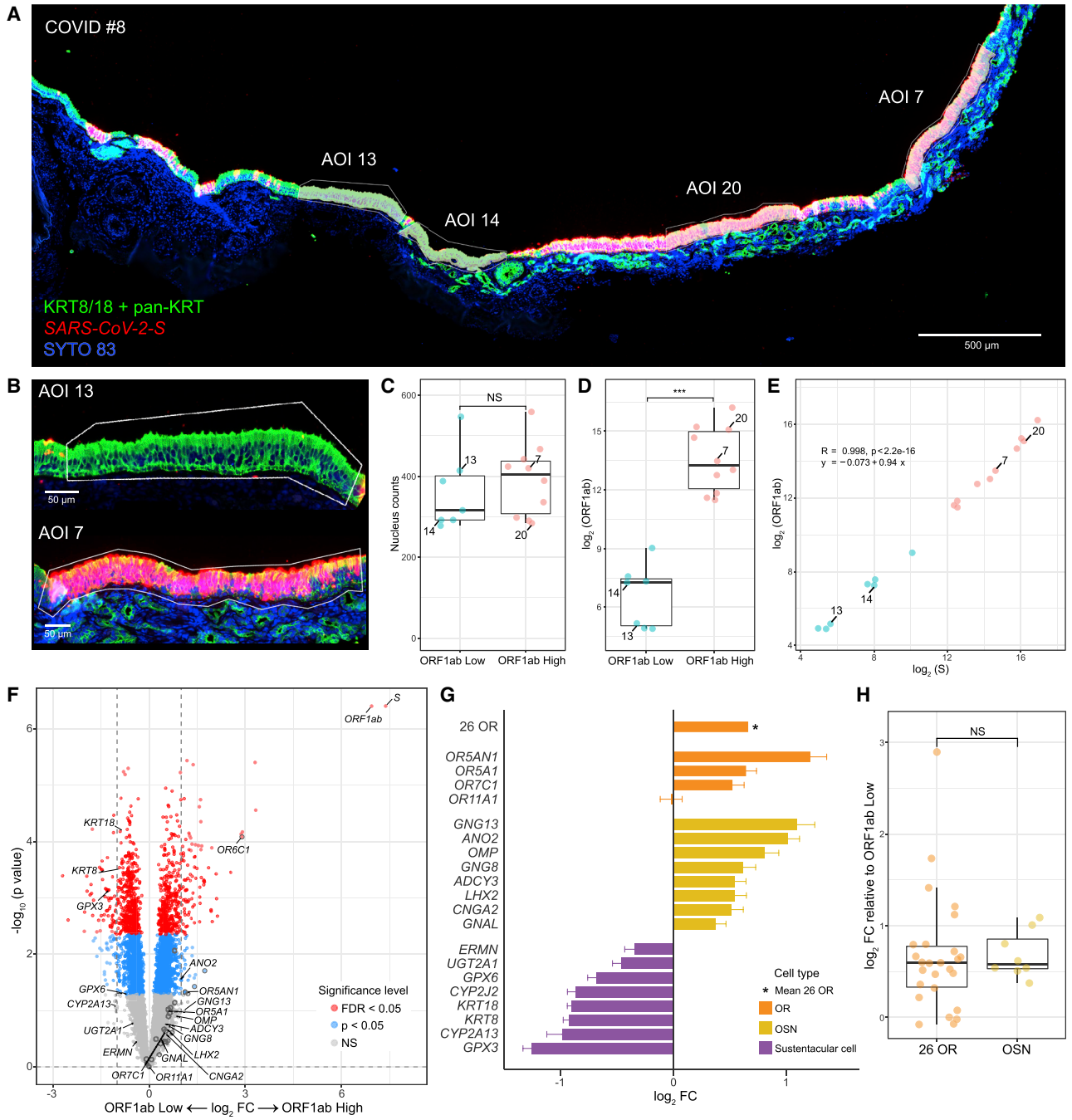

Figure 6. Spatial whole-transcriptome profiling of the olfactory epithelium in COVID-19

(A) Scanned image of a section through the OM of COVID #8. RNAscope for *S* was combined with IHC for KRT8/18 and pan-KRT. Four AOIs in the OE are indicated, with a low viral load (13 and 14) or a high viral load (20 and 7). SYTO 83 served as nuclear stain.

(B) Magnification of AOI 13 and AOI 7.

(C) Boxplots of nucleus counts of AOIs with low versus high viral load, with the numbers of the four AOIs shown in (A). NS, not significant.

(D) Boxplots of $\log_2$ normalized expression counts for *orf1ab* (p = 7.96e-07).

(E) Regression curve between normalized expression counts for *S* (x axis) and *orf1ab* (y axis).

(F) Volcano plot with the magnitude expressed as $\log_2$ FC (x axis) and significance expressed as $-\log_{10}$ of the unadjusted p value (y axis) of differential expression of 9,262 genes (dots) in WTA data between the ten ORF1ab High AOIs and the seven ORF1ab Low AOIs. Dashed vertical lines represent a $|\log_2 FC|$ of one. Genes of interest are labeled. Dots with gray outlines are the 26 OR genes. Dots with p values with a false discovery rate (FDR) <5% are shown in red.

(G) Log_2 FC values of markers for sustentacular cells (bottom) and OSNs (middle) and of OR genes (top). The asterisk indicates the average of the 26 differentially expressed OR genes.

(H) Boxplots of $\log_2$ normalized expression counts for the 26 differentially expressed OR genes (26 OR) and the 8 OSN markers (OSN).

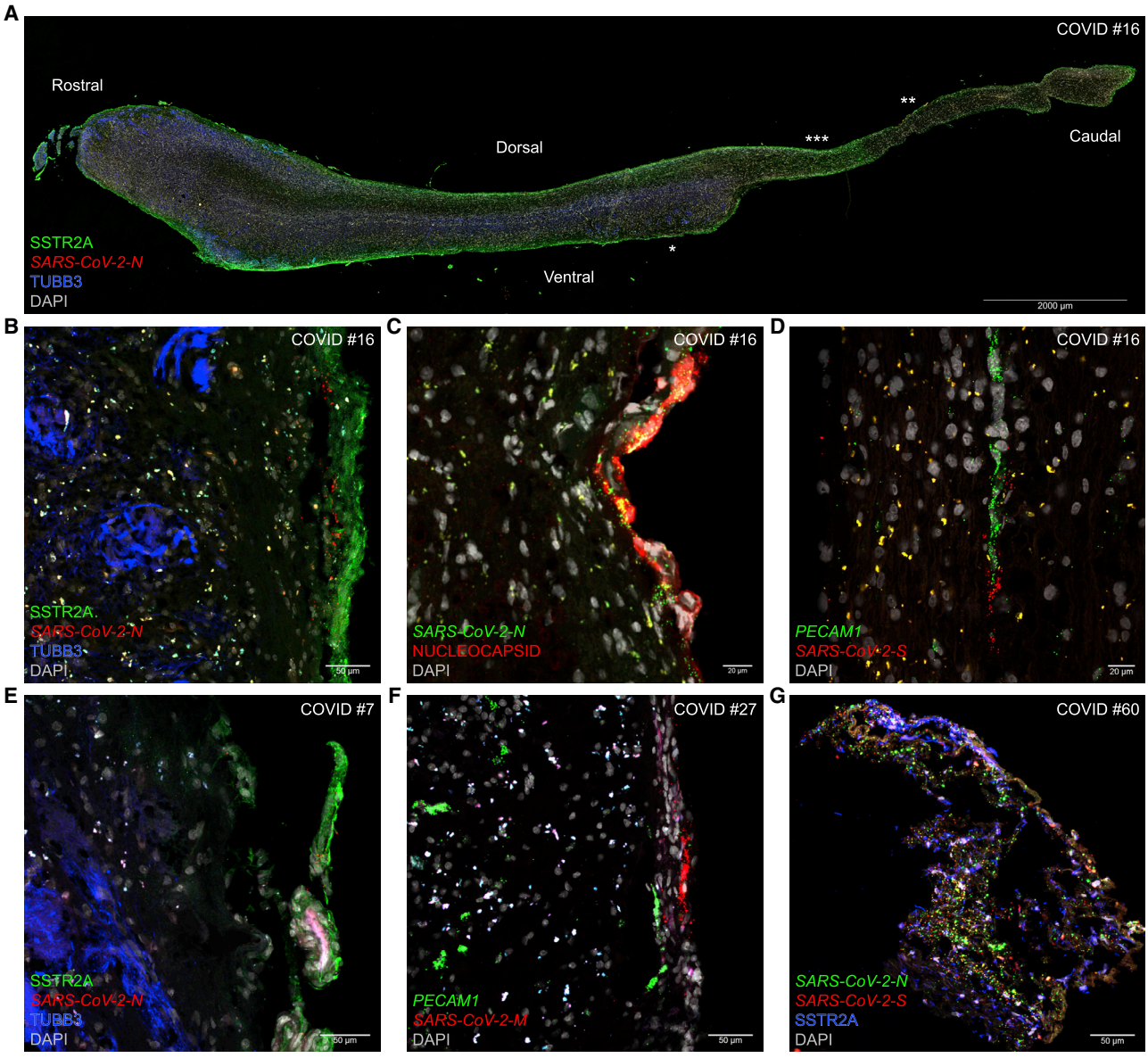

Figure 7. The parenchyma of the olfactory bulb is spared from infection

(A–D) Confocal images of sagittal sections through an OB of COVID #16. The SSTR2A-IR signal labels leptomeninges, and the TUBB3-IR signal labels OSN axons and OB neurons. *N* puncta are not visible in the tiled confocal image (A), with the single asterisk indicating a position in this section (B), and double asterisks and triple asterisks positions in adjacent sections (C) and (D). *N* puncta occur within the side of pia mater abutting the OB (B). *N* puncta are dispersed over an area of the pia mater containing abundant nucleocapsid-IR signal (C). *PECAM1* labels endothelial cells of a blood vessel cut obliquely, and *S* puncta occur within its lumen (D).

(E) Sagittal section through an OB of COVID #7. *N* puncta occur within a swath of the pia mater that is partially detached.

(F) Sagittal section through an OB of COVID #27. The pia mater contains densely packed *M* puncta. *PECAM1* puncta occur in endothelial cells of a blood vessel within the pia mater and blood vessels within the OB.

(G) Section through the leptomeninges including the transition zone to dura mater of COVID #60 shows scattered *N* and *S* puncta.

DAPI served as nuclear stain. See also Figure S2.

Catching SARS-CoV-2 in the act of attacking the nasal mucosa

Our cohort consisted of patients who died from or with COVID-19 in two major hospitals over a period of 12 months spanning the first three waves of the pandemic in Belgium. We consistently kept the PMI at approximately one hour. None of the 85 cases had to be excluded because of poor staining quality. As the onset of symptoms is not always clear or even known and is subject to patient recall, we chose to report the period until death starting from the time the NP swab was taken that led to the diagnosis.

The 30 informative cases died at a median of 8.8 days (Q1–Q3: 4–12) after diagnosis, compared to 21.1 days (Q1–Q3: 11–37) for the 38 non-informative cases (Mann-Whitney U test, $U = 144$, $z = -5.26$, $p < 0.001$). The two convalescent COVID-19 patients, who died several months after recovering, did not have detectable viral RNA or nucleocapsid-IR in the tissue samples. One of them, COVID #3, was the donor for a successful bilateral lung transplantation (Ceulemans et al., 2021a). We detected *N* and *S* puncta in a postmortem lung biopsy of COVID #3 (Ceulemans et al., 2021b) but not in the RM, OM, and OB.

Of the 30 informative cases, 9 (30%) displayed ongoing viral replication at the time of death, as judged by the presence of *sense* puncta: COVID #7, #8, #27, #39, #51, #60, #63, #67, and #68. These patients died within 8.5 days after diagnosis. Our panel of seven RNAscope probes and the nucleocapsid antibody represents a stringent criterion for assessing virus replication. As sustentacular cells have phagocytic activity (Suzuki et al., 1996), the mere demonstration of nucleocapsid-IR signal (or spike-IR signal) in sustentacular cells is insufficient to call these cells infected: the signal may reflect phagocytosis of debris from infected cells.

Infection of sustentacular cells

The major target cell type in the RM are ciliated cells (Ahn et al., 2021; Hou et al., 2020; Lee et al., 2020; Sungnak et al., 2020; Ziegler et al., 2021). The objective of our extensive examination of the RM samples was to provide suitable context for the examination of the olfactory cleft mucosa samples, in view of the scattered distribution of OM as an archipelago of islands within an ocean of RM. The patchiness of the infection gets superimposed on the scattered distribution of OM. In the six COVID-19 cases with viral RNA and nucleocapsid-IR signal in OM islands that unmistakably contain OSNs, we also detected viral RNA and nucleocapsid-IR signal in the RM samples.

The major target cell type in the OM are sustentacular cells. These non-neuronal cells have glia-like properties and are regenerated throughout life from stem cells in the OE. Due to the scarcity of literature about human sustentacular cells (Morrison and Costanzo, 1990, 1992), it is not known to which extent the properties of sustentacular cells of laboratory rodents (Costanzo and Morrison, 1989) resemble those of humans. Rodent sustentacular cells have been ascribed myriad roles collectively referred to as "supporting": absorptive, detoxifying, metabolic, nourishing, phagocytic, physical, secretory, structural. One model, in rats, proposes that sustentacular cells take up glucose from blood vessels in the LP basally and secrete it into the mucus apically to fuel OSN cilia (Acevedo et al., 2019; Villar et al., 2017, 2021). A cytoarchitectonic study in rats illustrated the enwrapment of multiple OSN dendrites within the apical half of a single sustentacular cell (Liang, 2018, 2020). In humans, a belt-like junctional complex connects adjacent sustentacular cells and OSNs (Morrison and Costanzo, 1990). Given these intimate associations, it would be unsurprising if OSNs become affected, structurally and/or physiologically, when sustentacular cells are infected by SARS-CoV-2.

That sustentacular cells might be susceptible to SARS-CoV-2 infection has been widely inferred from their expression of ACE2 and TMPRSS2. Our findings are consistent with these inferences. On the other hand, the human coronaviruses SARS-CoV and HCoV-NL63 also engage ACE2 as entry receptor but do not cause anosmia, with one exception for SARS-CoV (Hwang, 2006). Interestingly, all strains of the coronavirus mouse hepatitis virus use the same receptor for cell entry despite very different organ tropism (Weiss and Leibowitz, 2011). The expression pattern of the receptor can predict which cells can be infected but does not mean that all cells that express this receptor or even the cells with the highest expression level are the major targets (Weiss, 2020). A secretory form of ACE2 may explain some of these discrepancies (Yeung et al., 2021). Neuropilin-1 expression in olfactory epithelial cells has been invoked as a cofactor facilitating SARS-CoV-2 cell entry and infectivity (Cantuti-Castelvetri et al., 2020).

Absence of evidence for infection of OSNs

In the same vein, the popular interpretation of the absence of expression of ACE2 and TMPRSS2 by human OSNs has been that OSNs might not be susceptible to SARS-CoV-2 infection. Nonetheless, infection of sporadic OSNs has been suggested in living (de Melo et al., 2021) and deceased COVID-19 patients (Meinhardt et al., 2021). But the fractions of infected OSNs were extremely low, making it implausible that these sporadic events would give rise to anosmia. Unfortunately, 3A2, the sole SARS-CoV-2-S antibody used in two postmortem studies (Cantuti-Castelvetri et al., 2020; Meinhardt et al., 2021) may bind a specific, but non-SARS-CoV-2, antigen (Yang et al., 2021). Replication of SARS-CoV-2 in OSNs of COVID-19 patients has not been demonstrated.

We applied spatial whole-transcriptome profiling to the OE of COVID #8 to address quantitatively the hypothesis of an indirect effect on OR gene expression. This method is complementary and orthogonal to the RNAscope analysis. We took an analytical approach of intra-patient, intra-slide profiling, and interrogated multiple AOIs within the OE. Our interpretation of the GeoMx WTA data is that the relative contribution of RNA from the infected subpopulation of sustentacular cells is reduced in AOIs with high versus low viral loads. The nonstructural protein nsp1 of SARS-CoV-2 elicits a rapid decay of host mRNAs (Burke et al., 2021; Finkel et al., 2021), consistent with our observations that infected sustentacular cells are low in or devoid of puncta for marker genes such as *UGT2A1*, *GPX3*, and *SOX2*. An AOI can be regarded as a tiny, directed biopsy of a few hundred cells, and expression counts of RNA from an AOI are normalized. Therefore, the anti-correlated increase in normalized expression counts for OSN marker genes does not reflect upregulation of gene expression in OSNs but mRNA decay in infected sustentacular cells. OR genes do not undergo changes in gene expression—neither down nor up. To confirm and extend these findings, it will be necessary to investigate cases of patients who died later after diagnosis and still had OE that was infected.

Admittedly, the absence of evidence for infection of OSNs does not constitute evidence of absence. We leave the possibility open that OSNs may become infected and support viral replication in a subset of patients, or in certain disease courses or phases.

Leptomeningeal viral RNA presence does not necessarily equal neuroinvasion

OSNs do not appear to offer SARS-CoV-2 a route straight to the brain from the nasal cavity via the OB. An intriguing observation was our finding of *SARS-CoV-2* puncta in the leptomeningeal layers surrounding the OB in 11 of the 30 informative cases. We speculate that these puncta reflect RNA within free extracellular virions instead of intracellular viral RNA synthesized by infected cells prior to budding. The absence of *sense* puncta argues against ongoing viral replication at these sites. These virions may have arrived at the leptomeninges via the cerebrospinal fluid, which flows within the subarachnoid space. They may have made it to the cranial cavity via the olfactory nerve after all, but then rather by hitchhiking on it paracellularly than migrating intracellularly through OSN axons. Alternatively, leptomeningeal virions may have taken a hematogenous route and be secondary to viremia, with virions spilling over from meningeal blood vessels (Thakur et al., 2021) into the cerebrospinal fluid. An explanation with fewer pathological implications is that the viral puncta merely reflect RNAemia (Järhult et al., 2021), viral RNA sequences floating around in the blood, be it whole genomes or fragments thereof. These virions may remain largely outside cells and not cause inflammation, consistent with the paucity of clinical reports about meningitis in COVID-19 patients. But they may cause neurological sequelae in a subset of patients (Balcom et al., 2021), such as by prompting the generation of autoantibodies against neural antigens (Song et al., 2021a). It is tempting to speculate that this viral RNA presence may contribute to olfactory dysfunction by perturbing signal propagation via the olfactory tract from the OB to the cerebral cortex.

Here too, the absence of evidence for invasion of the OB parenchyma does not equal evidence of absence of invasion. In any case, our data do not support the neurotropic properties and neuroinvasive capacity that have been attributed by some to SARS-CoV-2 (Song et al., 2021b).

A look ahead

The pathogenesis of olfactory dysfunction in COVID-19 may turn out to be multifactorial and heterogeneous among patients. There need not be a single mechanism explaining all cases of olfactory dysfunction. We favor a pathobiological mechanism whereby the sequence of events that ultimately mutes or alters the sense of smell is initiated when infected sustentacular cells no longer provide sufficient support, structural and/or physiological, to OSNs. They may even harm OSNs, such as through paracrine effects of chemokines secreted as part of the antiviral response. The OE is a functional unit consisting of a neuronal component (OSNs) and a non-neuronal component (sustentacular cells), with both components regenerated from stem cells throughout life (basal cells). The olfactory dysfunction usually being transient, recovery of the sense of smell would ensue when a newly generated cohort of sustentacular cells resumes support of OSNs.

The 23andMe COVID-19 initiative reported on a genome-wide association study comparing loss of smell or taste with no loss of smell or taste among nearly 70,000 probands with a positive SARS-CoV-2 test (Shelton et al., 2021). A single associated locus was identified, comprising the *UGT2A1* and *UGT2A2* genes encoding UDP glucuronosyltransferase enzymes. In rat, UGT2A1 is involved in odorant metabolization, which aids in olfactory signal termination (Lazard et al., 1991). Our findings of *UGT2A1* puncta support a role of sustentacular cells in COVID-19-associated olfactory dysfunction.

In view of the superficial location of sustentacular cells, which present ACE2 receptors to virions within the mucus, the mucosal immune system (Iwasaki, 2016) may not be able to prevent infection of these cells. It may have to condone a brief phase of viral replication in sustentacular cells of convalescent COVID-19 patients during re-infection or fully vaccinated individuals during breakthrough infection (Yewdell, 2021). Therefore, prior natural infection or vaccination may not be fully protective against olfactory dysfunction upon subsequent exposure to SARS-CoV-2.

Conclusions

Understanding the mechanisms whereby human sustentacular cells normally support OSNs in countless ways may yield clues for therapeutic interventions aimed at preventing, alleviating, or curing olfactory dysfunction in COVID-19. The spotlight ought to be shone on the unsung heroes of the sense of smell—the humble sustentacular cells.

Limitations of the study

The scope of the study was limited to visualizing how SARS-CoV-2 attacks the nasal mucosa and whether it invades the OB parenchyma. We took the viewpoint of the virus and not of the host. The sequence of pathobiological events leading to olfactory dysfunction may include an inflammatory component (Kirschenbaum et al., 2020). Irreparable tissue damage at the level of the OM (Fodoulian et al., 2020; Vaira et al., 2020a) may underlie the persistent anosmia observed in a subset of COVID-19 patients (Cecchini et al., 2021; Renaud et al., 2021).

Objective evaluation of olfactory function of COVID-19 patients during their time in the hospital was not available. Logistically, it is impractical to safely and adequately conduct smell tests on critically ill patients in a COVID-19 ICU or ward, and impossible when they are sedated and mechanically ventilated. Subjective evaluation of olfactory function is unreliable: there are discrepancies between self-reporting versus testing of the sense of smell in patients presenting with olfactory dysfunction (Hummel et al., 2017) and in COVID-19 patients (Mazzatenta et al., 2020; Vaira et al., 2020b). A fundamental limitation of studies of olfactory dysfunction in COVID-19 is that it may have preceded the infection: typically, objective baseline data are not available.

Quantification of the extent of the infection was not carried out as there are no validated methods to quantify the anatomical scattering of OM islands and the density of sustentacular cells and OSNs in the human OE. Moreover, the patchiness of the infection is superimposed on the scattered distribution of OM.

The spatial whole-transcriptome profiling was limited to a single case, COVID #8, a patient who died 4 days after diagnosis. Conceivably, changes in OR gene expression may manifest themselves later in the course of the infection. Longitudinal postmortem studies are obviously not possible, and each case represents a snapshot in an individual course of infection.

STAR★METHODS

Detailed methods are provided in the online version of this paper and include the following:

- KEY RESOURCES TABLE
- RESOURCE AVAILABILITY
  - Lead contact
  - Materials availability
  - Date and code availability
- EXPERIMENTAL MODEL AND SUBJECT DETAILS
  - Study design and data collection
  - Clinical parameters
- METHOD DETAILS
  - Tissue sampling
  - Rapid antigen tests and PCR tests on postmortem nasopharyngeal swabs
  - Sample processing
  - H&E staining
  - RNAscope *in situ* hybridization
  - Immunohistochemistry
  - BaseScope *in situ* hybridization
  - Spatial whole-transcriptome profiling
- QUANTIFICATION AND STATISTICAL ANALYSIS
  - Spatial whole-transcriptome profiling
  - Mann-Whitney U test

SUPPLEMENTAL INFORMATION

Supplemental information can be found online at https://doi.org/10.1016/j.cell.2021.10.027.

ACKNOWLEDGMENTS

We thank the nurses, doctors, and staff of the COVID-19 ICUs and wards of the University Hospitals Leuven and the General Hospital Sint-Jan Brugge-Oostende and the transplant coordination team of the University Hospitals Leuven for their unwavering support and enthusiastic cooperation; Bart De Beir, Olivia Dimanski, Ling Li, Florian Lindenblatt, and Erick Rea Escalante for technical support; Patrick Meeze and Tillman Suhr for drawings; Ayse Dereli for inspiring discussions; and Thomas Boehm, Nils-Göran Larsson, and Bert Vandeloo for comments on a draft of the manuscript. C.V. and L.V.G. were supported by post-doctoral grants from the University Hospitals Leuven (KOOR-UZ Leuven). J.W. and L.V.G. were supported by Research Foundation Flanders (FWO): Senior Clinical Investigator Fellowship 1833317N and 18B2222N respectively. P.M. acknowledges the financial support of the Max Planck Society.

AUTHOR CONTRIBUTIONS

P.M. and L.V.G. conceived and designed the study and supervised the project throughout the project, from bed to bench. M.J., L.V.G., C.V., J.G., Y.D., M.P., J.W., L.M., P.D.M., N.L., M.C., W.B., P.V.B., A.V., K.S., C.L., and M.B. collected tissue samples and/or clinical data. M.K., S.-J.Y., S.C., and H.Z. generated RNAscope/IHC data. M.K. generated confocal and brightfield images. T.D.H., A.N., L.P., and J.D.R. generated and analyzed DSP data. P.M. wrote the original draft of the manuscript. M.K., M.C., W.B., C.V., D.R.T., A.N., K.L., and L.V.G. revised the manuscript. All authors edited the manuscript.

DECLARATION OF INTERESTS

T.D.H., A.N., L.P., and J.W.R. are employees and stockholders at NanoString Technologies, Inc.

Received: June 29, 2021
Revised: September 1, 2021
Accepted: October 25, 2021
Published: November 3, 2021

REFERENCES

Acevedo, C., Blanchard, K., Bacigalupo, J., and Vergara, C. (2019). Possible ATP trafficking by ATP-shuttles in the olfactory cilia and glucose transfer across the olfactory mucosa. FEBS Lett. *593*, 601–610.

Ahn, J.H., Kim, J., Hong, S.P., Choi, S.Y., Yang, M.J., Ju, Y.S., Kim, Y.T., Kim, H.M., Rahman, M.D.T., Chung, M.K., et al. (2021). Nasal ciliated cells are primary targets for SARS-CoV-2 replication in the early stage of COVID-19. J. Clin. Invest. *131*, e148517.

Balcom, E.F., Nath, A., and Power, C. (2021). Acute and chronic neurological disorders in COVID-19: potential mechanisms of disease. Brain. Published online August 16, 2021. https://doi.org/10.1093/brain/awab302.

Banerjee, A.K., Blanco, M.R., Bruce, E.A., Honson, D.D., Chen, L.M., Chow, A., Bhat, P., Ollikainen, N., Quinodoz, S.A., Loney, C., et al. (2020). SARS-CoV-2 disrupts splicing, translation, and protein trafficking to suppress host defenses. Cell *183*, 1325–1339.

Barnes, I.H.A., Ibarra-Soria, X., Fitzgerald, S., Gonzalez, J.M., Davidson, C., Hardy, M.P., Manthravadi, D., Van Gerven, L., Jorissen, M., Zeng, Z., et al. (2020). Expert curation of the human and mouse olfactory receptor gene repertoires identifies conserved coding regions split across two exons. BMC Genomics *21*, 196.

Beechem, J.M. (2020). High-plex spatially resolved RNA and protein detection using Digital Spatial Profiling: a technology designed for immuno-oncology biomarker discovery and translational research. Methods Mol. Biol. *2055*, 563–583.

Boulagnon-Rombi, C., Fleury, C., Fichel, C., Lefour, S., Marchal Bressenot, A., and Gauchotte, G. (2017). Immunohistochemical approach to the differential diagnosis of meningiomas and their mimics. J. Neuropathol. Exp. Neurol. *76*, 289–298.

Brann, D.H., Tsukahara, T., Weinreb, C., Lipovsek, M., Van den Berge, K., Gong, B., Chance, R., Macaulay, I.C., Chou, H.J., Fletcher, R.B., et al. (2020). Non-neuronal expression of SARS-CoV-2 entry genes in the olfactory system suggests mechanisms underlying COVID-19-associated anosmia. Sci. Adv. *6*, eabc5801.

Brant, A.C., Tian, W., Majerciak, V., Yang, W., and Zheng, Z.M. (2021). SARS-CoV-2: from its discovery to genome structure, transcription, and replication. Cell Biosci. *11*, 136.

Buck, L., and Axel, R. (1991). A novel multigene family may encode odorant receptors: a molecular basis for odor recognition. Cell *65*, 175–187.

Burke, J.M., St Clair, L.A., Perera, R., and Parker, R. (2021). SARS-CoV-2 infection triggers widespread host mRNA decay leading to an mRNA export block. RNA *27*, 1318–1329.

Butowt, R., Meunier, N., Bryche, B., and von Bartheld, C.S. (2021). The olfactory nerve is not a likely route to brain infection in COVID-19: a critical review of data from humans and animal models. Acta Neuropathol. *141*, 809–822.

Cantuti-Castelvetri, L., Ojha, R., Pedro, L.D., Djannatian, M., Franz, J., Kuivanen, S., van der Meer, F., Kallio, K., Kaya, T., Anastasina, M., et al. (2020). Neuropilin-1 facilitates SARS-CoV-2 cell entry and infectivity. Science *370*, 856–860.

Cecchini, M.P., Brozzetti, L., Cardobi, N., Sacchetto, L., Gibellini, D., Montemezzi, S., Cheli, M., Manganotti, P., Monaco, S., and Zanusso, G. (2021). Persistent chemosensory dysfunction in a young patient with mild COVID-19 with partial recovery 15 months after the onset. Neurol. Sci. Published online October 2, 2021. https://doi.org/10.1007/s10072-021-05635-y.

Ceulemans, L.J., Van Slambrouck, J., De Leyn, P., Decaluwé, H., Van Veer, H., Depypere, L., Ceuterick, V., Verleden, S.E., Vanstapel, A., Desmet, S., et al. (2021a). Successful double-lung transplantation from a donor previously infected with SARS-CoV-2. Lancet Respir. Med. *9*, 315–318.

Ceulemans, L.J., Khan, M., Yoo, S.J., Zapiec, B., Van Gerven, L., Van Slambrouck, J., Vanstapel, A., Van Raemdonck, D., Vos, R., Wauters, E., et al. (2021b). Persistence of SARS-CoV-2 RNA in lung tissue after mild COVID-19. Lancet Respir. Med. *9*, e78–e79.

Chandrashekar, A., Liu, J., Martinot, A.J., McMahan, K., Mercado, N.B., Peter, L., Tostanoski, L.H., Yu, J., Maliga, Z., Nekorchuk, M., et al. (2020). SARS-CoV-2 infection protects against rechallenge in rhesus macaques. Science *369*, 812–817.

Cooper, K.W., Brann, D.H., Farruggia, M.C., Bhutani, S., Pellegrino, R., Tsukahara, T., Weinreb, C., Joseph, P.V., Larson, E.D., Parma, V., et al. (2020). COVID-19 and the chemical senses: Supporting players take center stage. Neuron *107*, 219–233.

Costanzo, R.M., and Morrison, E.E. (1989). Three-dimensional scanning electron microscopic study of the normal hamster olfactory epithelium. J. Neurocytol. *18*, 381–391.

Davies, N.G., Abbott, S., Barnard, R.C., Jarvis, C.I., Kucharski, A.J., Munday, J.D., Pearson, C.A.B., Russell, T.W., Tully, D.C., Washburne, A.D., et al.; CMMID COVID-19 Working Group; COVID-19 Genomics UK (COG-UK) Consortium (2021). Estimated transmissibility and impact of SARS-CoV-2 lineage B.1.1.7 in England. Science *372*, eabg3055.

de Melo, G.D., Lazarini, F., Levallois, S., Hautefort, C., Michel, V., Larrous, F., Verillaud, B., Aparicio, C., Wagner, S., Gheusi, G., et al. (2021). COVID-19-related anosmia is associated with viral persistence and inflammation in human olfactory epithelium and brain infection in hamsters. Sci. Transl. Med. *13*, eabf8396.

Delorey, T.M., Ziegler, C.G.K., Heimberg, G., Normand, R., Yang, Y., Segerstolpe, Å., Abbondanza, D., Fleming, S.J., Subramanian, A., Montoro, D.T., et al. (2021). COVID-19 tissue atlases reveal SARS-CoV-2 pathology and cellular targets. Nature *595*, 107–113.

Durante, M.A., Kurtenbach, S., Sargi, Z.B., Harbour, J.W., Choi, R., Kurtenbach, S., Goss, G.M., Matsunami, H., and Goldstein, B.J. (2020). Single-cell analysis of olfactory neurogenesis and differentiation in adult humans. Nat. Neurosci. *23*, 323–326.

Eliezer, M., Hautefort, C., Hamel, A.L., Verillaud, B., Herman, P., Houdart, E., and Eloit, C. (2020). Sudden and complete olfactory loss of function as a possible symptom of COVID-19. JAMA Otolaryngol. Head Neck Surg. *146*, 674–675.

Engström, H., and Bloom, G. (1953). The structure of the olfactory region in man. Acta Otolaryngol. *43*, 11–21.

Escada, P. (2013). [Localization and distribution of human olfactory mucosa in the nasal cavities]. Acta Med. Port. *26*, 200–207.

Favre, J.J., Chaffanjon, P., Passagia, J.G., and Chirossel, J.P. (1995). Blood supply of the olfactory nerve. Meningeal relationships and surgical relevance. Surg. Radiol. Anat. *17*, 133–138, 12–14.

Finkel, Y., Gluck, A., Nachshon, A., Winkler, R., Fisher, T., Rozman, B., Mizrahi, O., Lubelsky, Y., Zuckerman, B., Slobodin, B., et al. (2021). SARS-CoV-2 uses a multipronged strategy to impede host protein synthesis. Nature *594*, 240–245.

Fodoulian, L., Tuberosa, J., Rossier, D., Boillat, M., Kan, C., Pauli, V., Egervari, K., Lobrinus, J.A., Landis, B.N., Carleton, A., and Rodriguez, I. (2020). SARS-CoV-2 receptors and entry genes are expressed in the human olfactory neuroepithelium and brain. iScience *23*, 101839.

Fung, T.S., and Liu, D.X. (2019). Human coronavirus: host-pathogen Interaction. Annu. Rev. Microbiol. *73*, 529–557.

Gagliardi, S., Emanuele Poloni, T., Pandini, C., Garofalo, M., Dragoni, F., Medici, V., Davin, A., Damiana Visonà, S., Moretti, M., Sproviero, D., et al. (2021). Detection of SARS-CoV-2 genome and whole transcriptome sequencing in frontal cortex of COVID-19 patients. Brain Behav. Immun. *97*, 13–21.

Hofmann, H., Pyrc, K., van der Hoek, L., Geier, M., Berkhout, B., and Pöhlmann, S. (2005). Human coronavirus NL63 employs the severe acute respiratory syndrome coronavirus receptor for cellular entry. Proc. Natl. Acad. Sci. USA *102*, 7988–7993.

Holbrook, E.H., Leopold, D.A., and Schwob, J.E. (2005). Abnormalities of axon growth in human olfactory mucosa. Laryngoscope *115*, 2144–2154.

Holbrook, E.H., Wu, E., Curry, W.T., Lin, D.T., and Schwob, J.E. (2011). Immunohistochemical characterization of human olfactory tissue. Laryngoscope *121*, 1687–1701.

Hou, Y.J., Okuda, K., Edwards, C.E., Martinez, D.R., Asakura, T., Dinnon, K.H., 3rd, Kato, T., Lee, R.E., Yount, B.L., Mascenik, T.M., et al. (2020). SARS-CoV-2 reverse genetics reveals a variable infection gradient in the respiratory tract. Cell *182*, 429–446.

Hummel, T., Whitcroft, K.L., Andrews, P., Altundag, A., Cinghi, C., Costanzo, R.M., Damm, M., Frasnelli, J., Gudziol, H., Gupta, N., et al. (2017). Position paper on olfactory dysfunction. Rhinol. Suppl. *54*, 1–30.

Hwang, C.S. (2006). Olfactory neuropathy in severe acute respiratory syndrome: report of A case. Acta Neurol. Taiwan. *15*, 26–28.

Iwasaki, A. (2016). Exploiting mucosal immunity for antiviral vaccines. Annu. Rev. Immunol. *34*, 575–608.

Jaeger, S.R., McRae, J.F., Bava, C.M., Beresford, M.K., Hunter, D., Jia, Y., Chheang, S.L., Jin, D., Peng, M., Gamble, J.C., et al. (2013). A Mendelian trait for olfactory sensitivity affects odor experience and food selection. Curr. Biol. *23*, 1601–1605.

Järhult, J.D., Hultström, M., Bergqvist, A., Frithiof, R., and Lipcsey, M. (2021). The impact of viremia on organ failure, biomarkers and mortality in a Swedish cohort of critically ill COVID-19 patients. Sci. Rep. *11*, 7163.

Jerby-Arnon, L., Neftel, C., Shore, M.E., Weisman, H.R., Mathewson, N.D., McBride, M.J., Haas, B., Izar, B., Volorio, A., Boulay, G., et al. (2021). Opposing immune and genetic mechanisms shape oncogenic programs in synovial sarcoma. Nat. Med. *27*, 289–300.

Jones, T.C., Biele, G., Mühlemann, B., Veith, T., Schneider, J., Beheim-Schwarzbach, J., Bleicker, T., Tesch, J., Schmidt, M.L., Sander, L.E., et al. (2021). Estimating infectiousness throughout SARS-CoV-2 infection course. Science *373*, eabi5273.

Kachramanoglou, C., Law, S., Andrews, P., Li, D., and Choi, D. (2013). Culture of olfactory ensheathing cells for central nerve repair: the limitations and potential of endoscopic olfactory mucosal biopsy. Neurosurgery *72*, 170–178, discussion, 178–179.

Kassam, A., Snyderman, C.H., Mintz, A., Gardner, P., and Carrau, R.L. (2005). Expanded endonasal approach: the rostrocaudal axis. Part I. Crista galli to the sella turcica. Neurosurg. Focus *19*, E3.

Kern, R.C. (2000). Chronic sinusitis and anosmia: pathologic changes in the olfactory mucosa. Laryngoscope *110*, 1071–1077.

Kim, D., Lee, J.Y., Yang, J.S., Kim, J.W., Kim, V.N., and Chang, H. (2020). The architecture of SARS-CoV-2 transcriptome. Cell *181*, 914–921.

Kirschenbaum, D., Imbach, L.L., Ulrich, S., Rushing, E.J., Keller, E., Reimann, R.R., Frauenknecht, K.B.M., Lichtblau, M., Witt, M., Hummel, T., et al. (2020). Inflammatory olfactory neuropathy in two patients with COVID-19. Lancet *396*, 166.

Lazard, D., Zupko, K., Poria, Y., Nef, P., Lazarovits, J., Horn, S., Khen, M., and Lancet, D. (1991). Odorant signal termination by olfactory UDP glucuronosyl transferase. Nature *349*, 790–793.

Lechien, J.R., Chiesa-Estomba, C.M., Beckers, E., Mustin, V., Ducarme, M., Journe, F., Marchant, A., Jouffe, L., Barillari, M.R., Cammaroto, G., et al. (2021). Prevalence and 6-month recovery of olfactory dysfunction: a multicentre study of 1363 COVID-19 patients. J. Intern. Med. *290*, 451–461.

Lee, M.K., Tuttle, J.B., Rebhun, L.I., Cleveland, D.W., and Frankfurter, A. (1990). The expression and posttranslational modification of a neuron-specific β-tubulin isotype during chick embryogenesis. Cell Motil. Cytoskeleton *17*, 118–132.

Lee, I.T., Nakayama, T., Wu, C.T., Goltsev, Y., Jiang, S., Gall, P.A., Liao, C.K., Shih, L.C., Schürch, C.M., McIlwain, D.R., et al. (2020). ACE2 localizes to the respiratory cilia and is not increased by ACE inhibitors or ARBs. Nat. Commun. *11*, 5453.

Liang, F. (2018). Olfactory receptor neuronal dendrites become mostly intrasustentacularly enwrapped upon maturity. J. Anat. *232*, 674–685.

Liang, F. (2020). Sustentacular cell enwrapment of olfactory receptor neuronal dendrites: an update. Genes (Basel) *11*, 493.

Liu, J., Babka, A.M., Kearney, B.J., Radoshitzky, S.R., Kuhn, J.H., and Zeng, X. (2020). Molecular detection of SARS-CoV-2 in formalin-fixed, paraffin-embedded specimens. JCI Insight *5*, e139042.

López-Elizalde, R., Campero, A., Sánchez-Delgadillo, T., Lemus-Rodríguez, Y., López-González, M.I., and Godínez-Rubí, M. (2018). Anatomy of the olfactory nerve: A comprehensive review with cadaveric dissection. Clin. Anat. *31*, 109–117.

Lüers, J.C., Klußmann, J.P., and Guntinas-Lichius, O. (2020). Die COVID-19-Pandemie und das HNO-Fachgebiet: Worauf kommt es aktuell an? Laryngo-rhinootologie *99*, 287–291.

Martin, D.P., Weaver, S., Tegally, H., San, J.E., Shank, S.D., Wilkinson, E., Lucaci, A.G., Giandhari, J., Naidoo, S., Pillay, Y., et al.; NGS-SA; COVID-19 Genomics UK (COG-UK) (2021). The emergence and ongoing convergent evolution of the SARS-CoV-2 N501Y lineages. Cell *184*, 5189–5200.

Matschke, J., Lütgehetmann, M., Hagel, C., Sperhake, J.P., Schröder, A.S., Edler, C., Mushumba, H., Fitzek, A., Allweiss, L., Dandri, M., et al. (2020). Neuropathology of patients with COVID-19 in Germany: a post-mortem case series. Lancet Neurol. *19*, 919–929.

Mazzatenta, A., Neri, G., D'Ardes, D., De Luca, C., Marinari, S., Porreca, E., Cipollone, F., Vecchiet, J., Falcicchia, C., Panichi, V., et al. (2020). Smell and taste in severe CoViD-19: Self-reported vs. testing. Front. Med. (Lausanne) *7*, 589409.

Meinhardt, J., Radke, J., Dittmayer, C., Franz, J., Thomas, C., Mothes, R., Laue, M., Schneider, J., Brünink, S., Greuel, S., et al. (2021). Olfactory transmucosal SARS-CoV-2 invasion as a port of central nervous system entry in individuals with COVID-19. Nat. Neurosci. *24*, 168–175.

Menke, J.R., Raleigh, D.R., Gown, A.M., Thomas, S., Perry, A., and Tihan, T. (2015). Somatostatin receptor 2a is a more sensitive diagnostic marker of meningioma than epithelial membrane antigen. Acta Neuropathol. *130*, 441–443.

Merritt, C.R., Ong, G.T., Church, S.E., Barker, K., Danaher, P., Geiss, G., Hoang, M., Jung, J., Liang, Y., McKay-Fleisch, J., et al. (2020). Multiplex digital spatial profiling of proteins and RNA in fixed tissue. Nat. Biotechnol. *38*, 586–599.

Morrison, E.E., and Costanzo, R.M. (1990). Morphology of the human olfactory epithelium. J. Comp. Neurol. *297*, 1–13.

Morrison, E.E., and Costanzo, R.M. (1992). Morphology of olfactory epithelium in humans and other vertebrates. Microsc. Res. Tech. *23*, 49–61.

Naessen, R. (1970). The identification and topographical localisation of the olfactory epithelium in man and other mammals. Acta Otolaryngol. *70*, 51–57.

Patel, B.V., Haar, S., Handslip, R., Auepanwiriyakul, C., Lee, T.M., Patel, S., Harston, J.A., Hosking-Jervis, F., Kelly, D., Sanderson, B., et al.; United Kingdom COVID-ICU National Service Evaluation (2021). Natural history, trajectory, and management of mechanically ventilated COVID-19 patients in the United Kingdom. Intensive Care Med. *47*, 549–565.

Peacock, T.P., Penrice-Randal, R., Hiscox, J.A., and Barclay, W.S. (2021). SARS-CoV-2 one year on: evidence for ongoing viral adaptation. J. Gen. Virol. *102*, 001584.

Pinna, Fde.R., Ctenas, B., Weber, R., Saldiva, P.H., and Voegels, R.L. (2013). Olfactory neuroepithelium in the superior and middle turbinates: which is the optimal biopsy site? Int. Arch. Otorhinolaryngol. *17*, 131–138.

Renaud, M., Thibault, C., Le Normand, F., Mcdonald, E.G., Gallix, B., Debry, C., and Venkatasamy, A. (2021). Clinical outcomes for patients with anosmia 1 year after COVID-19 diagnosis. JAMA Netw. Open *4*, e2115352.

Salazar, I., Sanchez-Quinteiro, P., Barrios, A.W., López Amado, M., and Vega, J.A. (2019). Anatomy of the olfactory mucosa. Handb. Clin. Neurol. *164*, 47–65.

Schubert, K., Karousis, E.D., Jomaa, A., Scaiola, A., Echeverria, B., Gurzeler, L.A., Leibundgut, M., Thiel, V., Mühlemann, O., and Ban, N. (2020). SARS-CoV-2 Nsp1 binds the ribosomal mRNA channel to inhibit translation. Nat. Struct. Mol. Biol. *27*, 959–966.

Shelton, J.F., Shastri, A.J., The 23andMe COVID-19 Team, Aslibekyan, S., and Auton, A. (2021). The UGT2A1/UGT2A2 locus is associated with COVID-19-related anosmia. medRxiv. Published online May 31, 2021. https://doi.org/10.1101/2021.05.28.21257993.

Sola, I., Almazán, F., Zúñiga, S., and Enjuanes, L. (2015). Continuous and discontinuous RNA synthesis in coronaviruses. Annu. Rev. Virol. *2*, 265–288.

Song, E., Bartley, C.M., Chow, R.D., Ngo, T.T., Jiang, R., Zamecnik, C.R., Dandekar, R., Loudermilk, R.P., Dai, Y., Liu, F., et al. (2021a). Divergent and self-reactive immune responses in the CNS of COVID-19 patients with neurological symptoms. Cell Rep Med *2*, 100288.

Song, E., Zhang, C., Israelow, B., Lu-Culligan, A., Prado, A.V., Skriabine, S., Lu, P., Weizman, O.E., Liu, F., Dai, Y., et al. (2021b). Neuroinvasion of SARS-CoV-2 in human and mouse brain. J. Exp. Med. *218*, e20202135.

Sudre, C.H., Keshet, A., Graham, M.S., Joshi, A.D., Shilo, S., Rossman, H., Murray, B., Molten, E., Klaser, K., Canas, L.D., et al. (2021). Anosmia, ageusia, and other COVID-19-like symptoms in association with a positive SARS-CoV-2 test, acrosssix national digital surveillance platforms: an observational study. Lancet Digit Health *3*, e577–e586. https://doi.org/10.1016/S2589-7500(21)00115-1.

Sungnak, W., Huang, N., Bécavin, C., Berg, M., Queen, R., Litvinukova, M., Talavera-López, C., Maatz, H., Reichart, D., Sampaziotis, F., et al.; HCA Lung Biological Network (2020). SARS-CoV-2 entry factors are highly expressed in nasal epithelial cells together with innate immune genes. Nat. Med. *26*, 681–687.

Suzuki, Y., Takeda, M., and Farbman, A.I. (1996). Supporting cells as phagocytes in the olfactory epithelium after bulbectomy. J. Comp. Neurol. *376*, 509–517.

Tanos, T., Saibene, A.M., Pipolo, C., Battaglia, P., Felisati, G., and Rubio, A. (2017). Isolation of putative stem cells present in human adult olfactory mucosa. PLoS One *12*, e0181151.

Thakur, K.T., Miller, E.H., Glendinning, M.D., Al-Dalahmah, O., Banu, M.A., Boehme, A.K., Boubour, A.L., Bruce, S.S., Chong, A.M., Claassen, J., et al. (2021). COVID-19 neuropathology at Columbia University Irving Medical Center/New York Presbyterian Hospital. Brain *144*, 2696–2708.

V'kovski, P., Kratzel, A., Steiner, S., Stalder, H., and Thiel, V. (2021). Coronavirus biology and replication: implications for SARS-CoV-2. Nat. Rev. Microbiol. *19*, 155–170.

Vaira, L.A., Hopkins, C., Sandison, A., Manca, A., Machouchas, N., Turilli, D., Lechien, J.R., Barillari, M.R., Salzano, G., Cossu, A., et al. (2020a). Olfactory epithelium histopathological findings in long-term coronavirus disease 2019 related anosmia. J. Laryngol. Otol. *134*, 1123–1127.

Vaira, L.A., Salzano, G., Deiana, G., and De Riu, G. (2020b). Anosmia and ageusia: common findings in COVID-19 patients. Laryngoscope *130*, 1787.

Vaira, L.A., Lechien, J.R., Khalife, M., Petrocelli, M., Hans, S., Distinguin, L., Salzano, G., Cucurullo, M., Doneddu, P., Salzano, F.A., et al. (2021). Psychophysical evaluation of the olfactory function: European multicenter study on 774 COVID-19 patients. Pathogens *10*, 62.

Van Aerde, N., Van den Berghe, G., Wilmer, A., Gosselink, R., and Hermans, G.; COVID-19 Consortium (2020). Intensive care unit acquired muscle weakness in COVID-19 patients. Intensive Care Med. *46*, 2083–2085.

van der Hoek, L., Pyrc, K., Jebbink, M.F., Vermeulen-Oost, W., Berkhout, R.J., Wolthers, K.C., Wertheim-van Dillen, P.M., Kaandorp, J., Spaargaren, J., and Berkhout, B. (2004). Identification of a new human coronavirus. Nat. Med. *10*, 368–373.

Van Gerven, L., Hellings, P.W., Cox, T., Fokkens, W., Hopkins, C., Hox, V., Jorissen, M., Schuermans, A., Sinonquel, P., Speleman, K., et al. (2020). Personal protection and delivery of rhinologic and endoscopic skull base procedures during the COVID-19 outbreak. Rhinology *58*, 289–294.

Vasvári, G., Reisch, R., and Patonay, L. (2005). Surgical anatomy of the cribriform plate and adjacent areas. Minim. Invasive Neurosurg. *48*, 25–33.

Villar, P.S., Delgado, R., Vergara, C., Reyes, J.G., and Bacigalupo, J. (2017). Energy requirements of odor transduction in the chemosensory cilia of olfactory sensory neurons rely on oxidative phosphorylation and glycolytic processing of extracellular glucose. J. Neurosci. *37*, 5736–5743.

Villar, P.S., Vergara, C., and Bacigalupo, J. (2021). Energy sources that fuel metabolic processes in protruding finger-like organelles. FEBS J. *288*, 3799–3812.

Wang, F., Flanagan, J., Su, N., Wang, L.C., Bui, S., Nielson, A., Wu, X., Vo, H.T., Ma, X.J., and Luo, Y. (2012). RNAscope: a novel in situ RNA analysis platform for formalin-fixed, paraffin-embedded tissues. J. Mol. Diagn. *14*, 22–29.

Wang, C., Horby, P.W., Hayden, F.G., and Gao, G.F. (2020). A novel coronavirus outbreak of global health concern. Lancet *395*, 470–473.

Weiss, S.R. (2020). Forty years with coronaviruses. J. Exp. Med. *217*, e20200537.

Weiss, S.R., and Leibowitz, J.L. (2011). Coronavirus pathogenesis. Adv. Virus Res. *81*, 85–164.

Whitcroft, K.L., and Hummel, T. (2020). Olfactory dysfunction in COVID-19: diagnosis and management. JAMA *323*, 2512–2514.

Wölfel, R., Corman, V.M., Guggemos, W., Seilmaier, M., Zange, S., Müller, M.A., Niemeyer, D., Jones, T.C., Vollmar, P., Rothe, C., et al. (2020). Virological assessment of hospitalized patients with COVID-2019. Nature *581*, 465–469.

Xydakis, M.S., Dehgani-Mobaraki, P., Holbrook, E.H., Geisthoff, U.W., Bauer, C., Hautefort, C., Herman, P., Manley, G.T., Lyon, D.M., and Hopkins, C. (2020). Smell and taste dysfunction in patients with COVID-19. Lancet Infect. Dis. *20*, 1015–1016.

Xydakis, M.S., Albers, M.W., Holbrook, E.H., Lyon, D.M., Shih, R.Y., Frasnelli, J.A., Pagenstecher, A., Kupke, A., Enquist, L.W., and Perlman, S. (2021). Post-viral effects of COVID-19 in the olfactory system and their implications. Lancet Neurol. *20*, 753–761.

Yang, A.C., Kern, F., Losada, P.M., Agam, M.R., Maat, C.A., Schmartz, G.P., Fehlmann, T., Stein, J.A., Schaum, N., Lee, D.P., et al. (2021). Dysregulation of brain and choroid plexus cell types in severe COVID-19. Nature *595*, 565–571.

Yeung, M.L., Teng, J.L.L., Jia, L., Zhang, C., Huang, C., Cai, J.P., Zhou, R., Chan, K.H., Zhao, H., Zhu, L., et al. (2021). Soluble ACE2-mediated cell entry of SARS-CoV-2 via interaction with proteins related to the renin-angiotensin system. Cell *184*, 2212–2228.

Yewdell, J.W. (2021). Individuals cannot rely on COVID-19 herd immunity: Durable immunity to viral disease is limited to viruses with obligate viremic spread. PLoS Pathog. *17*, e1009509.

Zapiec, B., Dieriks, B.V., Tan, S., Faull, R.L.M., Mombaerts, P., and Curtis, M.A. (2017). A ventral glomerular deficit in Parkinson's disease revealed by whole olfactory bulb reconstruction. Brain *140*, 2722–2736.

Zhang, K., Miorin, L., Makio, T., Dehghan, I., Gao, S., Xie, Y., Zhong, H., Esparza, M., Kehrer, T., Kumar, A., et al. (2021). Nsp1 protein of SARS-CoV-2 disrupts the mRNA export machinery to inhibit host gene expression. Sci. Adv. *7*, eabe7386.

Ziegler, C.G., Miao, V.N., Owings, A.H., Navia, A.W., Tang, Y., Bromley, J.D., Lotfy, P., Sloan, M., Laird, H., Williams, H.B., et al. (2021). Impaired local intrinsic immunity to SARS-CoV-2 infection in severe COVID-19. Cell *184*, 4713–4733.

Zou, L., Ruan, F., Huang, M., Liang, L., Huang, H., Hong, Z., Yu, J., Kang, M., Song, Y., Xia, J., et al. (2020). SARS-CoV-2 viral load in upper respiratory specimens of infected patients. N. Engl. J. Med. *382*, 1177–1179.

Zugaj, M., van Ditzhuijzen, N.S., Golebski, K., and Fokkens, W.J. (2021). The effect of coronaviruses on olfaction: systematic review. Rhinology *59*, 226–235.

STAR★METHODS

KEY RESOURCES TABLE

Reagent or resource	Source	Identifier
Antibodies		
Goat Anti-Human ACE-2 Polyclonal antibody	R&D Systems	Cat#AF933; RRID: AB_355722
Rabbit monoclonal Cytokeratin 5/6 antibody (RM341)	Novus Biologicals	Cat#NBP2-77439; RRID: AB_2892200
Mouse monoclonal Cytokeratin 7 antibody (KRT7/760)	Novus Biologicals	Cat#NBP2-44813; RRID: AB_2892201
Mouse monoclonal anti-human Cytokeratin 8 antibody (LP3K)	R&D Systems	Cat#MAB3165; RRID: AB_2234521
Mouse monoclonal human Cytokeratin 18 antibody (810811)	R&D Systems	Cat#MAB7619; RRID: AB_2893116
Rabbit monoclonal anti-EpCAM antibody (E144)	Abcam	Cat#ab32392; RRID: AB_732181
Rabbit polyclonal ERMN antibody	Thermo Fisher Scientific	Cat#PA5-58327; RRID: AB_2641113
Mouse monoclonal MUC5AC antibody (45M1)	Thermo Fisher Scientific	Cat#MA5-12178; RRID: AB_10978001
Rabbit monoclonal SARS-CoV/SARS-CoV-2 Nucleocapsid antibody (clone #001)	Sino Biological	Cat#40143-R001; RRID: AB_2827974
Rabbit polyclonal antiserum Somatostatin receptor subtype 2A	Biotrend	Cat#NB-49-016-50ul
Mouse monoclonal anti-Tubulin beta 3/ TUBB3 (TUJ1)	BioLegend	Cat#801202; RRID: AB_10063408
Mouse monoclonal anti-pan-Cytokeratin (AE-1/AE-3), Alexa Fluor 488 Conjugated	Novus Biologicals	Cat#NBP2-33200AF488
Mouse monoclonal anti-Cytokeratin 8/18 (K8.8+DC10), Alexa Fluor 488 Conjugated	Novus Biologicals	Cat#NBP2-34655AF488
Donkey Anti-Rabbit IgG (H+L) Antibody, Alexa Fluor 488 Conjugated	Molecular Probes	Cat#A-21206; RRID: AB_2535792
Donkey anti-Mouse IgG (H+L) Highly Cross-Adsorbed Secondary Antibody, Alexa Fluor Plus 488	Thermo Fisher Scientific	Cat#A32766; RRID: AB_2762823
Donkey anti-Rabbit IgG (H+L) Highly Cross-Adsorbed Secondary Antibody, Alexa Fluor 546	Thermo Fisher Scientific	Cat#A10040, RRID: AB_2534016
Donkey Anti-Goat IgG (H+L) Antibody, Alexa Fluor 546 Conjugated	Molecular Probes	Cat#A-11056; RRID: AB_142628
Donkey anti-Rabbit IgG (H+L) Highly Cross-Adsorbed Secondary Antibody, Alexa Fluor Plus 555	Thermo Fisher Scientific	Cat#A32794; RRID: AB_2762834
Donkey anti-Mouse IgG (H+L) Highly Cross-Adsorbed Secondary Antibody, Alexa Fluor Plus 555	Thermo Fisher Scientific	Cat#A32773; RRID: AB_2762848
Donkey anti-Rabbit IgG (H+L) Highly Cross-Adsorbed Secondary Antibody, Alexa Fluor Plus 647	Thermo Fisher Scientific	Cat#A32795; RRID: AB_2762835
Donkey anti-Mouse IgG (H+L) Highly Cross-Adsorbed Secondary Antibody, Alexa Fluor Plus 647	Thermo Fisher Scientific	Cat#A32787; RRID: AB_2762830

(*Continued on next page*)

Continued

Reagent or resource	Source	Identifier
Biological samples		
Nasal mucosae and olfactory bulbs from COVID-19 patients and control patients	Ethical Committee of the University Hospitals Leuven, Leuven, Belgium (S64042) and the General Hospital Sint-Jan Brugge-Oostende AV in Bruges, Belgium (2736)	clinicaltrials.gov (NCT04445597)
Chemicals, peptides, and recombinant proteins		
Mount Solid antifade	abberior	Cat#MM-2011-2X15ML
RNAscope Target Retrieval Reagent	Advanced Cell Diagnostics	Cat#322000
RNAscope Protease III	Advanced Cell Diagnostics	Cat#322337
RNAscope Probe Diluent	Advanced Cell Diagnostics	Cat#300041
10% neutral buffered formalin	Sigma-Aldrich	Cat#HT5011
10% neutral buffered formalin	Electron Microscopy Sciences	Cat#15740-04
Tissue-Tek O.C.T. compound	Sakura	Cat#4583
Opal 520	Akoya Biosciences	Cat#FP1487001KT
Opal 570	Akoya Biosciences	Cat#FP1488001KT
Opal 690	Akoya Biosciences	Cat#FP1497001KT
1x Plus Amplification Diluents	Akoya Biosciences	Cat#FP1498
Donkey serum	Sigma-Aldrich	Cat#S30-100ML
Sucrose	Sigma-Aldrich	Cat#S0389-1KG
Agencourt AMPure XP	Beckman Coulter	Cat#A63880
SYTO 83 orange fluorescent nucleic acid stain	Thermo Fisher Scientific	Cat#S11364
DAPI (4',6-Diamidino-2-Phenylindole, Dihydrochloride)	Thermo Fisher Scientific	Cat#D1306
VectaMount permanent mounting medium	Vector Labs	Cat#H-5000
Critical commercial assays		
RNAscope Multiplex Fluorescent Detection Kit v2	Advanced Cell Diagnostics	Cat#323110
RNAscope 4-Plex Ancillary Kit	Advanced Cell Diagnostics	Cat#323120
RNAscope 3-plex Negative Control Probe	Advanced Cell Diagnostics	Cat#320871
BaseScope Duplex Reagent Kit	Advanced Cell Diagnostics	Cat#323800
RNAscope V-nCoV-N (C1)	Advanced Cell Diagnostics	Cat#846081
RNAscope V-nCoV-N (C2)	Advanced Cell Diagnostics	Cat#846081-C2
RNAscope V-nCoV-N (C3)	Advanced Cell Diagnostics	Cat#846081-C3
RNAscope V-nCoV2019-S (C1)	Advanced Cell Diagnostics	Cat#848561
RNAscope V-nCoV2019-S (C2)	Advanced Cell Diagnostics	Cat#848561-C2
RNAscope V-nCoV2019-S (C3)	Advanced Cell Diagnostics	Cat#848561-C3
RNAscope V-SARS-CoV-2003-S (C1)	Advanced Cell Diagnostics	Cat#860191
RNAscope V-nCoV-orf1ab-O1 (C1)	Advanced Cell Diagnostics	Cat#859981
RNAscope V-nCoV2019-S-sense (C1)	Advanced Cell Diagnostics	Cat#845701
RNAscope V-nCoV2019-S-sense (C2)	Advanced Cell Diagnostics	Cat#845701-C2
RNAscope V-nCoV2019-S-sense (C3)	Advanced Cell Diagnostics	Cat#845701-C3
RNAscope V-nCoV2019-orf1ab-sense (C1)	Advanced Cell Diagnostics	Cat#859151
RNAscope V-nCoV2019-orf1ab-sense (C2)	Advanced Cell Diagnostics	Cat#859151-C2
RNAscope V-SARS-CoV-2-N-O2-sense (C3)	Advanced Cell Diagnostics	Cat#863841-C3
RNAscope V-SARS-CoV-2-M (C2)	Advanced Cell Diagnostics	Cat#1046351-C2
RNAscope Hs-ANO2 (C4)	Advanced Cell Diagnostics	Cat#1047461-C4

(*Continued on next page*)

Continued

Reagent or resource	Source	Identifier
RNAscope Hs-CNGA2 (C3)	Advanced Cell Diagnostics	Cat#1031481-C3
RNAscope Hs-FOXJ1 (C2)	Advanced Cell Diagnostics	Cat#430921-C2
RNAscope Hs-FOXJ1 (C3)	Advanced Cell Diagnostics	Cat#430921-C3
RNAscope Hs-FOXJ1 (C4)	Advanced Cell Diagnostics	Cat#430921-C4
RNAscope Hs-GNAL (C1)	Advanced Cell Diagnostics	Cat#441751
RNAscope Hs-GNG13 (C1)	Advanced Cell Diagnostics	Cat#1003921-C1
RNAscope Hs-GPX3 (C2)	Advanced Cell Diagnostics	Cat#470591-C2
RNAscope Hs-OMP (C1)	Advanced Cell Diagnostics	Cat#824181
RNAscope Hs-OMP (C2)	Advanced Cell Diagnostics	Cat#824181-C2
RNAscope Hs-OMP (C3)	Advanced Cell Diagnostics	Cat#824181-C3
RNAscope Hs-OR5A1 (C3)	Advanced Cell Diagnostics	Cat#522261-C3
RNAscope Hs-OR5AN1 (C3)	Advanced Cell Diagnostics	Cat#1046301-C3
RNAscope Hs-OR7C1 (C4)	Advanced Cell Diagnostics	Cat#522271-C4
RNAscope Hs-OR11A1 (C2)	Advanced Cell Diagnostics	Cat#1046311-C2
RNAscope Hs-PECAM1-O1 (C1)	Advanced Cell Diagnostics	Cat#487381
RNAscope Hs-PECAM1-O1 (C4)	Advanced Cell Diagnostics	Cat#487381-C4
RNAscope Hs-SOX2 (C3)	Advanced Cell Diagnostics	Cat#400871-C3
RNAscope Hs-TMPRSS2 (C1)	Advanced Cell Diagnostics	Cat#470341
RNAscope Hs-UGT2A1 (C1)	Advanced Cell Diagnostics	Cat#814271
RNAscope 2.5 LS V-nCoV2019-S (C3)	Advanced Cell Diagnostics	Cat#848568-C3
BaseScope BA-V-SARS-CoV-2-orf1ab-SGFwt (C1)	Advanced Cell Diagnostics	Cat#1055881-C1
BaseScope BA-V-SARS-CoV-2-S-HVwt (C1)	Advanced Cell Diagnostics	Cat#1055861-C1
BaseScope BA-V-SARS-CoV-2-orf1ab-SGFdel (C2)	Advanced Cell Diagnostics	Cat#1055871-C2
BaseScope BA-V-SARS-CoV-2-S-HVdel (C2)	Advanced Cell Diagnostics	Cat#1055851-C2
GeoMx NGS RNA WTA Hs	NanoString Technologies	Cat#121401102
Panbio COVID-19 Rapid Test Device	Abbott	REF#41FK10
MagMAX Viral/Pathogen II Nucleic Acid Isolation Kit	Thermo Fisher Scientific	Cat#A48383
Applied Biosystems TaqPath COVID-19 RT-PCR kit	Thermo Fisher Scientific	Cat#A48067
Deposited data		
GeoMx DSP data at Gene Expression Omnibus (GEO)	This paper	https://www.ncbi.nlm.nih.gov/geo/query/acc.cgi?acc=GSE176080
Software and algorithms		
Zeiss ZEN 2.6 system	Zeiss	https://www.zeiss.com/corporate/int/home.html
GraphPad Prism v9.2	GraphPad	https://www.graphpad.com/
Adobe Illustrator 2020	Adobe	Adobe Creative Cloud
Adobe Acrobat Pro DC	Adobe	Adobe Creative Cloud
CaseViewer v2.4	3DHistech	http://www.sysmex-europe.com/products/products-detail/caseviewer.html
R version 4.1/development	R Foundation	https://www.r-project.org/
REACTOME_OLFACTORY_SIGNALING_PATHWAY gene set	https://www.gsea-msigdb.org/gsea/msigdb/cards/REACTOME_OLFACTORY_SIGNALING_PATHWAY	Systematic name: M4072

(*Continued on next page*)

Continued		
Reagent or resource	Source	Identifier
fgsea Bioconductor package	https://bioconductor.org/packages/release/bioc/html/fgsea.html	v1.17.0
org.Hs.eg.db Bioconductor database	https://bioconductor.org/packages/release/data/annotation/html/org.Hs.eg.db.html	v3.12.0
Other		
GeoMx Digital Spatial Profiler	NanoString Technologies	https://www.nanostring.com/products/geomx-digital-spatial-profiler/
Zeiss LSM 800	Zeiss	https://www.zeiss.com/corporate/int/home.html
PANNORAMIC MIDI II scanner	3DHistech	https://www.sysmex-europe.com/n/products/products-detail/pannoramic-midi-ii.html
Leica CM3050 S cryostat	Leica	https://www.leicabiosystems.com
Dako CoverStainer	Agilent	https://www.agilent.com

RESOURCE AVAILABILITY

Lead contact

Further information and requests should be directed to the Lead Contact, Peter Mombaerts (peter.mombaerts@gen.mpg.de).

Materials availability

This study did not generate new unique reagents.

Date and code availability

- Clinical data about the patients are confidential, subject to compliance with applicable personal data protection laws, and not publicly available. The GeoMx DSP data have been deposited at Gene Expression Omnibus and are publicly available as of the date of publication; the accession number is listed in the key resources table.
- This paper does not report original code.
- Any additional information required to reanalyze the data reported in this paper is available from the Lead Contact upon request.

EXPERIMENTAL MODEL AND SUBJECT DETAILS

Study design and data collection

The foundation of the study protocol ANOSMIC-19 (ANalyzing Olfactory dySfunction Mechanisms in COVID-19) is the bedside procurement of postmortem tissue samples. This national multicenter study was approved by the Ethical Committee of the University Hospitals Leuven, Leuven, Belgium (S64042) and the General Hospital Sint-Jan Brugge-Oostende AV in Bruges, Belgium (2736), and registered on clinicaltrials.gov (NCT04445597). The *Ethikrat – Kommission des Präsidenten* of the Max Planck Society did not require a separate ethics review by a medical ethics committee (Applications No: 2020_14, 2020_30, and 2020_31). Patients were > 18 years old at the time of inclusion. Written informed consent from next of kin was obtained prior to tissue harvesting in accordance with the recommendations of the local Ethical Committee.

COVID-19 patients were diagnosed with a SARS-CoV-2 infection by PCR from a nasopharyngeal swab and died during their subsequent COVID-19 hospitalization, except for two convalescent cases (COVID #3 and COVID #66), who died of other causes in a hospital months later. For COVID #2, the PCR diagnosis was done from a sample of bronchoalveolar lavage fluid. Control patients had a negative PCR test from a nasopharyngeal swab taken a few days prior to their time of death and died of other causes than COVID-19. The electronic health records of each patient were retrospectively reviewed and analyzed to obtain information about demographics, comorbidities, disease course, and hospitalization history. For a patient who was initially called control #11, diagnosis of COVID-19 was made postmortem by PCR on a nasopharyngeal swab we took during the postmortem bedside surgical procedure and in parallel through our RNAscope and IHC analyses. We then renamed control #11 as COVID #63 but did not reassign number 11 to the next control case.

The collection, processing, and disclosure of personal data, such as patient demographic, health, and medical information, are subject to compliance with Regulation (EU) 2016/679, also referred as the General Data Protection Regulation, and the Belgian Law on the protection of natural persons regarding the processing of personal data. Therefore, combinations of data deemed to be identificatory to specific persons cannot be disclosed.

Clinical parameters

Comorbidities were categorized in accordance with international recommendations. Overweight is as a body mass index (BMI) > 25 kg/m^2, and obesity as a BMI $\geq$ 30 kg/m^2. Presence of diabetes mellitus type 2 includes previously known and newly diagnosed patients, based on Hb1Ac $\geq$ 6.5% or active treatment on admission. Former smokers, defined as having ceased smoking > 6 months prior to inclusion, are not considered smokers in Figure 1B. Hypertension is defined as grade 1 hypertension, or treatment with antihypertensive drugs. Chronic kidney disease is defined as the presence of kidney damage or a glomerular filtration rate of < 60 ml/min/1.73 m^2 for > 3 months. Chronic lung disease includes obstructive lung disease (chronic obstructive pulmonary disease, asthma), interstitial lung disease, pulmonary fibrosis, and pulmonary hypertension. Cardiovascular disease comprises heart conditions (such as valvular disease, heart failure, arrhythmias, cardiomyopathies, coronary artery disease), cerebrovascular antecedents, and history of pulmonary embolism.

Patients were considered immunocompromised if one of the following criteria was met: (1) an active oncological condition, defined as presence of a solid tumor or hematologic malignancy < 6 months prior to inclusion; (2) immunosuppressive drugs as maintenance therapy, including corticosteroids and chemotherapy; (3) recipient of a solid organ transplant.

For ICU patients, the Sequential Organ Failure Assessment (SOFA) score, the Acute Physiology And Chronic Health Evaluation II (APACHE II) score, and the arterial-to-inspired oxygen (P_{aO2}/F_{IO2}) ratio were calculated daily. The highest SOFA and APACHE II scores and lowest P_{aO2}/F_{IO2} ratio were extracted from the patient file as indicators of disease severity while on ICU.

The cause of death of COVID-19 patients was classified into one out of three categories. (1) Death from COVID-19: hypoxic respiratory failure secondary to COVID-19 pneumonia, fatal SARS-CoV-2 myocarditis, and early coagulopathic complications. (2) Death with COVID-19: cause of death not directly related to COVID-19 such as acute cardiac arrest, cerebrovascular accidents, deterioration of an oncological condition. (3) Death from COVID-19 sequelae: complications associated with prolonged hospitalization on an ICU, such as multi-organ failure, sepsis, or late coagulopathic conditions.

METHOD DETAILS

Tissue sampling

Samples of respiratory and olfactory cleft mucosa and whole olfactory bulbs were harvested bedside by ENT surgeons via an endoscopic endonasal approach soon after the death of the patient. A 4 mm 0° endoscope (Karl Storz), connected with a camera and monitor and light source, was used throughout the procedure allowing optimal visualization and assistance.

To harvest respiratory mucosa samples, the inferior turbinate, middle turbinate, and superior turbinate were resected bilaterally with Heymann nasal scissors.

- The inferior turbinate is attached to the lateral nasal wall over its entire length (5-6 cm). Prior to cutting its attachment, the inferior turbinate was in-fractured by a Cottle elevator allowing optimal positioning of the Heymann scissors.
- The middle and superior turbinates each have a vertical, anterior attachment to the skull base and a horizontal, more posterior attachment to the lateral nasal wall. For both turbinates, the anterior attachment was cut first with Heymann or endoscopic scissors, followed by the posterior attachment.
- To harvest the mucosa *in toto* from the resected turbinate bone, a dissection in the subperiosteal plane was performed with a Cottle elevator.
- Samples of each turbinate were transferred into separate pots containing 10% formalin.

To harvest olfactory cleft mucosa samples, the lining covering the olfactory cleft including the superior part of the septum and the cribriform plate was resected.

- An elliptical incision was made with a sickle knife running over the superior part of the septum, the cribriform plate and the area of the vertical attachment of the medial and superior turbinates, thus covering the full olfactory cleft region.
- A subperiosteal dissection was initiated with a sickle knife on the medial side (superior part of the septum) and lateral side (vertical attachment of the turbinates) simultaneously, progressively extending to the center (cribriform plate), where the mucosa is attached only by the remaining fila olfactoria.
- After transection and tearing of the fila olfactoria, the mucosa was harvested in one or a few pieces. All pieces were transferred into a single container with 10% formalin.

To harvest whole olfactory bulbs, an adapted transcribriform approach was performed at the end of the procedure.

- A bilateral total (anterior and posterior) ethmoidectomy after landmarking the frontal, maxillary, and sphenoidal sinuses was performed to obtain full exposure of the ventral skull base from the posterior wall of the frontal sinus until the anterior wall of the sphenoid. The width was maximally exposed from the lamina papyracea (the medial wall of the orbit) until the septum over the entire length. The position of the anterior and posterior ethmoidal arteries guided the orientation.
- After full exposure of the bony skull base, the adapted transcribriform approach was performed. Compared to the conventional approach, the opening made in the bony skull base is smaller: extending from lateral to the anterior attachment of the middle and superior turbinates until the septum (width) and from the anterior ethmoidal artery until the anterior wall of the sphenoid (length). Resection of the bony skull was performed with hammer and chisel. Cold instruments were used instead of powered instruments, such as a high-speed drill with rinsing system, to avoid aerosol formation in these patients, who might still have been contagious at the time of death.
- The exposed dura mater was incised longitudinally and paramedially to avoid damage to the overlying olfactory bulb. After the olfactory bulb was exposed, blunt resection with a ball probe allowed harvesting of the full length of the olfactory bulb, often including an attached part of the olfactory tract. Therefore, the transection was made as posteriorly as possible.

The ENT surgeons wore powered air-purifying respirator masks and personal protective equipment during the surgical procedure on COVID-19 patients.

Rapid antigen tests and PCR tests on postmortem nasopharyngeal swabs

In October 2020, the amended ANOSMIC-19 study protocol implemented systematically the use of rapid antigen tests (RATs) on nasopharyngeal swabs taken by the ENT surgeons from the deceased patients prior to the postmortem bedside surgical procedure. RATs were performed bedside on COVID cases #9 through #70 (89%) and control cases #8 through #16 (53%). We used the Panbio Abbott COVID-19 Rapid Test Device (Abbott, REF#41FK10), a membrane-based immunochromatography assay that detects the nucleocapsid protein of SARS-CoV-2 in nasopharyngeal samples.

From January 2021, a second nasopharyngeal swab was taken preprocedurally from 11 COVID-19 cases and stored at −80°C. Later RT-qPCR analysis was performed in the Department of Laboratory Medicine, University Hospitals Leuven, Leuven, Belgium, the Belgian national reference center for coronavirus analyses. Viral RNA extraction was performed with the MagMAX Viral/Pathogen II kit (Thermo Fisher Scientific, Cat#A48383) on a KingFisher Flex System, followed by qPCR with the TaqPath COVID-19 RT-PCR kit (Thermo Fisher Scientific, Cat#A48067) on a QuantStudio 7 Flex platform (Thermo Fisher Scientific).

Sample processing

Tissue samples from the 70 COVID-19 cases and the 15 control cases were transferred into containers with 10% neutral buffered formalin (Sigma-Aldrich, Cat#HT5011) for > 72 hr to fix the tissues and inactivate SARS-CoV-2. Samples were treated for cryoprotection by immersing serially in 15%, 25%, and 30% sucrose (Sigma-Aldrich, Cat#S0389-1KG) in 1 x PBS over a period of 6–8 days. The orientation of the samples was recorded before embedding in Tissue-Tek O.C.T. compound (Sakura, Cat#4583) on dry ice. Cryosections of 6–8 μm thickness were cut on a Leica CM3050 S cryostat and collected on SuperFrost Plus Gold slides (Thermo Fisher Scientific/Menzel Gläser, Cat#K5800AMNZ72). Slides were air-dried at room temperature, and boxes of slides were sealed prior to storage at −80°C.

H&E staining

Tissue sections were stained using a fully automated H&E platform (Dako CoverStainer, Agilent).

RNAscope *in situ* hybridization

The fluorescence RNAscope platform was used to visualize viral RNA in the 70 COVID-19 cases and in the 15 control cases. Most slides contained multiple sections. Staining was performed with the RNAscope manual assay using the Multiplex Fluorescent Detection Kit v2 (Advanced Cell Diagnostics, Cat#323110) according to manufacturer's protocols. Briefly, slides were dried at 55°C overnight, then pretreated with hydrogen peroxide, followed by permeabilization in target retrieval reagent (Advanced Cell Diagnostics, Cat#322000) for 3 min in a steamer, and digestion with Protease III (Advanced Cell Diagnostics, Cat#322337) at 40°C for 15 min. A combination of probes for target RNA detection was hybridized at 40°C for 2 hr. Probes in the C4 channel were developed with the RNAscope 4-Plex Ancillary Kit (Advanced Cell Diagnostics, Cat#323120). Signal amplification was followed by development of appropriate HRP channels with dyes Opal 520 (Akoya Biosciences, Cat#FP1487001KT), Opal 570 (Akoya Biosciences, Cat#FP1488001KT), and Opal 690 (Akoya Biosciences, Cat#FP1497001KT). Background staining was evaluated with a negative control: with a probe for the *dapB* gene of *Bacillus subtilis* strain SMY using the 3-plex Negative Control reagent (Advanced Cell Diagnostics, Cat#320871). DAPI (Thermo Fisher Scientific, Cat#D1306) served as nuclear stain. Slides were mounted in Mount Solid antifade (abberior, Cat#MM-2011-2X15ML). Confocal images were taken with the Zeiss ZEN 2.6 system on a Zeiss LSM 800.

Immunohistochemistry

For codetection of RNA and protein, IHC was performed after the final step of HRP blocker application in the RNAscope Multiplex Fluorescent Detection protocol. Slides were blocked in 10% donkey serum (Sigma-Aldrich, Cat#S30-100ML) in 0.1% Triton/PBS at

room temperature for 1 hr. The following primary antibodies were diluted in 2% donkey serum in 0.1% Triton/PBS and incubated at 4°C overnight: human ACE-2 (R&D Systems, Cat#AF933) at 1:100, EpCAM (Abcam, Cat#ab32392) at 1:100, ERMN (Thermo Fisher Scientific, Cat#PA5-58327) at 1:100, Cytokeratin 5/6 (Novus Biologicals, Cat#NBP2-77439) at 1:200, Cytokeratin 7 (Novus Biologicals, Cat#NBP2-44813) at 1:200, Cytokeratin 8 (R&D Systems, Cat#MAB3165) at 1:200, Cytokeratin 18 (R&D Systems, Cat#MAB7619) at 1:500, MUC5AC (Thermo Fisher Scientific, Cat#MA5-12178) at 1:200, SARS-CoV-2 Nucleocapsid (Sino Biological, Cat#40143-R001) at 1:100, Somatostatin receptor subtype 2A/SSTR2A (Biotrend, Cat#NB-49-016-50ul) at 1:4000, and TuJ1/TUBB3 (BioLegend, Cat#801202) at 1:100 for OM sections and 1:400 for OB sections. Slides were then washed in 0.1% Triton/PBS 3 × 5 min each followed by incubation with appropriate secondary antibodies at 1:500 in 2% normal donkey serum in 0.1% Triton/PBS at room temperature for 1 hr. Secondary antibodies were Alexa Fluor 488 donkey anti-rabbit (Molecular Probes, Cat#A-21206), Alexa Fluor Plus 488 donkey anti-mouse (Thermo Fisher Scientific, Cat#A32766), Alexa Fluor 546 donkey anti-rabbit (Thermo Fisher Scientific, Cat#A10040), Alexa Fluor 546 donkey anti-goat (Molecular Probes, Cat#A-11056), Alexa Fluor Plus 647 donkey anti-rabbit (Thermo Fisher Scientific, Cat#A32795), Alexa Fluor Plus 647 donkey anti-mouse (Thermo Fisher Scientific, Cat#A32787), Alexa Fluor Plus 555 donkey anti-rabbit (Thermo Fisher Scientific, Cat#A32794), and Alexa Fluor Plus 555 donkey anti-mouse (Thermo Fisher Scientific, Cat#A32773). Slides were washed in 0.1% Triton/PBS 3 × 5 min each followed by DAPI (Thermo Fisher Scientific, Cat#D1306) application for nuclei staining. Slides were mounted in Mount Solid antifade (abberior, Cat#MM-2011-2X15ML). For IHC only, slides were pretreated in target retrieval reagent (Advanced Cell Diagnostics, Cat#322000) for 3 min in a steamer. Primary antibody application, secondary antibody detection, DAPI staining, and mounting were performed as above. Confocal images were taken with the Zeiss ZEN 2.6 system on a Zeiss LSM 800.

BaseScope *in situ* hybridization

To differentiate between infection with the B.1.1.7/Alpha variant versus non-B.1.1.7/non-Alpha lineages, custom BaseScope probes were designed for a 9-nucleotide deletion encoding amino acids SGF 3675-3677 of the *ORF1ab* gene (Advanced Cell Diagnostics, Cat#1055881-C1 for wild-type and Cat#1055871-C2 for deletion) and a 6-nucleotide deletion encoding amino acids HV 69-70 of the *S* gene (Advanced Cell Diagnostics, Cat#1055861-C1 for wild-type and Cat#1055851-C2 for deletion). The BaseScope assay was performed according to manufacturer's protocols using the BaseScope Duplex Reagent Kit (Advanced Cell Diagnostics, Cat#323800). Tissue pretreatment was performed in the same way as in the fluorescence RNAscope experiments. Slides were mounted in VectaMount permanent mounting medium (Vector Labs, Cat#H-5000) and scanned using a PANNORAMIC MIDI II scanner (3DHistech) in brightfield mode.

Spatial whole-transcriptome profiling

Selection of AOIs and sequencing

The fixed frozen slide was baked at 37°C for 1 hr, fixed for 30 min in 10% neutral buffered formalin (Electron Microscopy Sciences, Cat#15740-04), and was processed through the RNAscope Leica Protocol using probe *V-nCoV2019-S* (Advanced Cell Diagnostics, Cat#848568-C3) and the GeoMx slide prep protocol on a Leica Bond Rxm. The slide was then incubated with GeoMx WTA (NanoString Technologies, Cat#121401102) and COVID-19 spike-in reagents at 37°C overnight to allow the probes to hybridize to their RNA targets. Following incubation, morphology marker antibodies anti-Pan-cytokeratin (Novus Biologicals, Cat#NBP2-33200AF488) referred to as pan-KRT, anti-cytokeratin 8/18 (Novus Biologicals, Cat#NBP2-34655AF488) referred to as KRT8/18, and DNA dye Syto 83 (Thermo Fisher Scientific, Cat#S11364) were applied at room temperature. The slide was loaded on a GeoMx instrument (NanoString Technologies) and Areas of Interest (AOIs) were identified. Ultraviolet light was shone through each individual AOI, and liberated probes were collected onto a microtiter plate. Each collection of oligonucleotide tags from a given AOI was indexed with i7xi5 unique dual indexes using the GeoMx SeqCode primers with 18 cycles of PCR. Indexed AOIs were pooled and purified into two rounds of AMPure XP (Beckman Coulter, Cat#A63880) PCR purification using a 1.2x bead:sample ratio. Samples were then sequenced on an Illumina NextSeq 2000. FASTQ files were filtered and demultiplexed using DND2.0 with the following parameters: quality trim score = 20, adaptor trim match length = 10, adaptor trim max mismatch = 3, barcode max mismatch = 1, stitching max mismatch = 2, dedup-hd = 1. DND is used to convert the raw FASTQ files to Digital Count Conversion (DCC) file format.

Data QC and processing

Individual DCC files were aggregated and checked for probe-level quality prior to data analysis. The data consist of two pools totaling 18,953 probes and 18,704 genes. For the WTA, each gene is mapped to a single probe. For the COVID-19 spike-in, which includes probes for *S* and *ORF1ab*, there were five probes per target. Target counts were generated for the multiple-probe genes by taking the geometric mean of their counts after removing probes that did not pass the Grubb's outlier test (alpha = 0.01). Sample-level quality control was also performed. Each sample was screened to ensure greater than 50% sequencing saturation. The negative probe geometric means for each sample were visually checked to ensure there were no pool dropouts.

For each sample, two values of Limit of Quantification (LOQ) were derived, one for each pool. LOQ for a given gene is defined as the geometric mean of pool-specific negative probes times the geometric standard deviation of negative probes raised to a power of 2 (i.e., LOQ2). These LOQ values were used as a basis of filtering genes that are expressed near background. We required that a given gene needed to be above LOQ2 in at least 20% (i.e, in $\geq$ 4 of the 17 AOIs). The filtered expression data were then normalized. Specifically, the 75th percentile of target counts for each AOI was computed and each of these values was divided by the geometric mean

of the 75th percentile values of all 17 AOIs to generate normalization factors. Targets count values for a given AOI were then divided by their sample-specific normalization factor. GeoMx profiling data are available on GEO at GSE176080.

QUANTIFICATION AND STATISTICAL ANALYSIS

Spatial whole-transcriptome profiling

In Figures 6A and 6B, the geometric mean of the $\log_2$ normalized *ORF1ab* expression (9.92) was used as the basis of bifurcating samples into ORF1ab Low AOIs (n = 7) and ORF1ab High AOIs (n = 10). In Figure 6C, a Welch Two Sample t test was used to determine whether there was a significant difference in nucleus counts between ORF1ab Low AOIs (n = 7) and ORF1ab High AOIs (n = 10). In Figure 6D, a Welch Two Sample t test was used to determine whether there was a significant difference in normalized $\log_2$ *ORF1ab* expression between ORF1ab Low AOIs (n = 7) and ORF1ab High AOIs (n = 10). In Figure 6E, a linear model using the base stats package in R was used to regress $\log_2$ normalized *ORF1ab* expression against $\log_2$ normalized *S* expression (n = 17 AOIs). In Figure 6F, differential expression analysis was performed for each gene by regressing the $\log_2$ normalized gene expression by viral load (two levels) using R. Raw p values were adjusted for multiple hypothesis testing using a Benjamini-Hochberg False Discovery Rate of 5% (https://www.jstor.org/stable/2346101?seq=1). In Figure 6G, a bar plot was presented in GraphPad Prism v9.2. In Figure 6H, a Welch Two Sample t test was used to determine whether there was a significant difference in $\log_2$ FC of 26 OR genes (*OR10A6, OR10G3, OR11A1, OR1D2, OR2A4, OR2A5, OR2AP1, OR51E2, OR52A5, OR52E4, OR56A4, OR5A1, OR5A2, OR5AN1, OR5AU1, OR5L1, OR5M1, OR5M10, OR5P3, OR6C1, OR7A5, OR7C1, OR7D4, OR7E24, OR8G1, OR9G4*) and eight OSN markers (*ADCY3, ANO2, CNGA2, GNAL, GNG13, GNG8, LHX2, OMP*) relative to the ORF1ab Low baseline.

Mann-Whitney U test

In the Discussion, an independent-samples Mann-Whitney U test was run to determine if there were significant differences in the time from diagnosis to death between informative cases (n = 30, median 8.8 days, IQR 7.4) and non-informative cases (n = 38, median 21.1 days, IQR 26.4), with n the number of cases in each group, and IQR the interquartile range. The statistical analysis was performed using IBM SPSS Statistics (Release 27.0.1.0).

Supplemental figures

Patient characteristics

	COVID-19						Convalescent		Control	
	Total (n=68)		ICU (n=37)		Ward (n=31)		COVID #3	COVID #66	Total (n=15)	
Age	80	(69–85)	71	(62–80)	85	(82–89)	70–79	60–69	60	(54–72)
Men	48	(71%)	28	(76%)	20	(65%)	No	No	9	(60%)
Medical history										
Body mass index	27	(24–30)	29	(27–31)	24	(22–27)			26	(24–30)
BMI < 25	24	(35%)	7	(19%)	17	(55%)	Yes	Yes	6	(40%)
BMI 25 – 30	27	(40%)	17	(46%)	10	(32%)			6	(40%)
BMI 30 – 40	14	(21%)	11	(30%)	3	(10%)			3	(20%)
BMI > 40	3	(4%)	2	(5%)	1	(3%)			0	(0%)
Diabetes mellitus	31	(46%)	18	(49%)	13	(42%)	No	Yes	3	(20%)
Type 1	1	(1%)	1	(3%)	0	(0%)	No	Yes	0	(0%)
Type 2	30	(44%)	17	(46%)	13	(42%)	No	No	3	(20%)
Hypertension	50	(74%)	27	(73%)	23	(74%)	No	Yes	12	(80%)
Chronic kidney disease	24	(35%)	8	(22%)	16	(52%)	No	No	2	(13%)
Cardiovascular disease	44	(65%)	21	(57%)	23	(74%)	No	Yes	8	(53%)
Chronic lung disease	26	(38%)	15	(41%)	11	(35%)	No	No	2	(13%)
Smoking	35	(51%)	21	(57%)	14	(45%)	No	Yes	6	(40%)
Current	9	(13%)	7	(19%)	2	(6%)	No	No	3	(20%)
Former	26	(38%)	14	(38%)	12	(39%)	No	Yes	3	(20%)
Immunocompromised state										
Active oncological condition	9	(13%)	5	(14%)	4	(13%)	No	No	2	(13%)
Organ transplant	4	(6%)	2	(5%)	2	(6%)	No	No	1	(7%)
Immunosuppresive medication	21	(31%)	13	(35%)	8	(26%)	No	Yes	1	(7%)

Disease characteristics

	Total (n=68)		ICU (n=37)		Ward (n=31)		COVID #3	COVID #66	Total (n=15)	
Days of symptoms before hospitalization	5	(1–7)	6	(3–8)	2	(1–5)				
COVID-19 diagnosis by PCR										
≤ 7 days prior to death	13	(19%)	5	(14%)	8	(26%)				
> 7 and ≤ 14 days	26	(38%)	7	(19%)	19	(61%)				
> 14 and ≤ 21 days	8	(12%)	4	(11%)	4	(13%)				
> 21 and ≤ 28 days	7	(10%)	7	(19%)	0	(0%)				
> 28 days	14	(21%)	14	(38%)	0	(0%)	Yes	Yes		
Days on COVID-19 ICU/Ward	11	(6–22)	21	(13–32)	8	(5–10)	0	6	7	(4–11)
Disease severity										
Highest SOFA score	14	(11–17)	14	(11–17)					15	(12–19)
Highest APACHE II score	25	(19–30)	25	(19–30)					20	(19–29)
Lowest P/F ratio	54	(47–64)	54	(47–64)					83	(69–117)
Respiratory support										
Non-invasive modalities	38	(56%)	7	(19%)	31	(100%)	No	Yes	0	(0%)
Conventional oxygen therapy	13	(19%)	0	(0%)	13	(42%)	No	Yes	0	(0%)
High flow nasal canula	25	(37%)	7	(19%)	18	(58%)	No	No	0	(0%)
Invasive mechanical ventilation	30	(44%)	30	(81%)	0	(0%)	No	No	14	(93%)
Proning	22	(32%)	22	(59%)	0	(0%)	No	No	1	(7%)
Extracorporeal membrane oxygenation	6	(9%)	6	(16%)	0	(0%)	No	No	0	(0%)
Pharmacological therapy										
Anticoagulation	66	(97%)	36	(97%)	30	(97%)	No	Yes	10	(67%)
Steroids	58	(85%)	33	(89%)	25	(81%)	No	No	6	(40%)
Antiviral	23	(34%)	16	(43%)	7	(23%)	No	No	0	(0%)
Antibiotics	60	(88%)	33	(89%)	27	(87%)	No	No	11	(73%)
Interleukin receptor modulators	3	(4%)	3	(8%)	0	(0%)	No	No	0	(0%)
Convalescent plasma	2	(3%)	2	(5%)	0	(0%)	No	No	0	(0%)
Cause of death										
from COVID-19	39	(57%)	14	(38%)	25	(81%)				
with COVID-19	7	(10%)	2	(5%)	5	(16%)				
sequelae	22	(32%)	21	(57%)	1	(3%)				

Procedure characteristics

	Total (n=68)		ICU (n=37)		Ward (n=31)		COVID #3	COVID #66	Total (n=15)	
Postmortem interval in minutes	71	(53–100)	67	(44–89)	85	(65–136)			89	(36–109)
< 50 min	15	(22%)	13	(35%)	2	(6%)	No	Yes	6	(40%)
50 – 100 min	36	(53%)	17	(46%)	19	(61%)	Yes	No	4	(27%)
100 – 200 min	14	(21%)	7	(19%)	7	(23%)			3	(20%)
> 200 min	3	(4%)	0	(0%)	3	(10%)			2	(13%)
Duration of procedure in minutes	58	(43–79)	54	(42–71)	60	(47–118)	62	112	49	(41–62)

Figure S1. Patient, disease, and procedure characteristics of the cohort of 68 COVID-19 patients, 2 convalescent patients, and 15 control patients, related to Figure 1

Convalescent cases COVID #3 and COVID #66 are listed separately because these patients recovered from COVID-19 and died of other causes in a hospital several months after recovering. Continuous variables (time variables and body mass index) are expressed as median (interquartile range: Q1–Q3), and count variables are expressed as percentages. SOFA, Sequential Organ Failure Assessment; APACHE II, Acute Physiology And Chronic Health Evaluation II; P/F ratio, arterial-to-inspired oxygen ratio (P_{aO2}/F_{IO2}); ICU, intensive care unit.

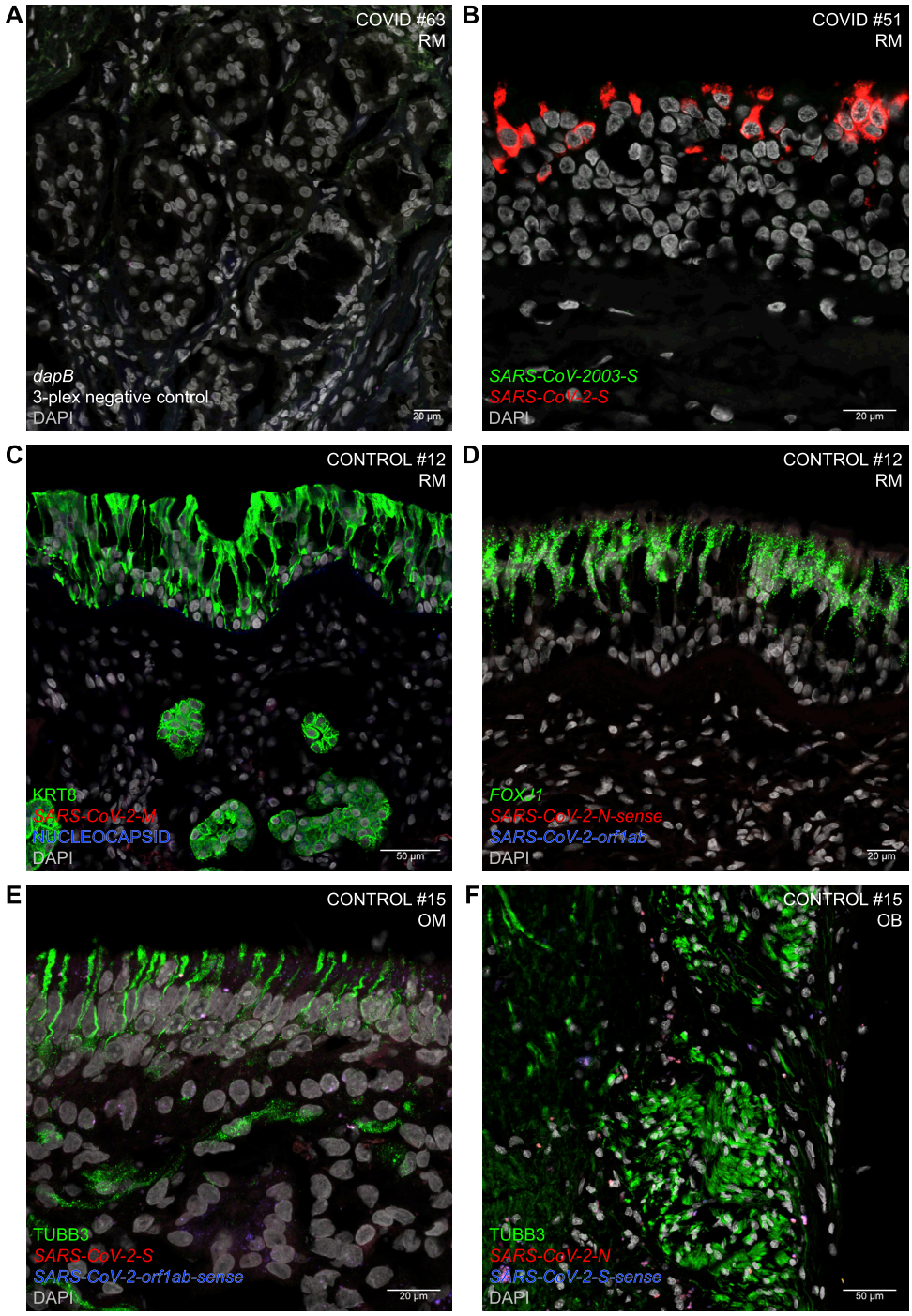

Figure S2. Negative control stainings, related to Figures 3, 5, and 7

(A) Confocal image of a section of the respiratory mucosa of COVID #63. A negative control for the RNAscope protocol was performed on a section adjacent to the section of which a confocal image is shown in Figure 3L. The specificity of the densely packed *SARS-CoV-2-orf1ab-sense* puncta in cells lining gland ducts in the lamina propria in Figure 3L is demonstrated by the absence of puncta for the *dapB* gene of *Bacillus subtilis* in any of the three Opal channels (3-plex). (B) Confocal image of a section of the respiratory mucosa of COVID #51. The *SARS-CoV-2-S* probe gives densely packed red puncta. The *SARS-CoV-2003-S* probe, specific for *S* of SARS-CoV (now known as SARS-CoV-1) causing an outbreak in 2002–2004, gives no green puncta. (C) Confocal image of a section of the respiratory mucosa of control #12. This negative control for the *SARS-CoV-2-M* probe and the nucleocapsid antibody reveals no red puncta or blue IR signal. KRT8 marks epithelial cells in the respiratory epithelium and the lamina propria. (D) Confocal image of a section of the respiratory mucosa of control #12. This negative control for the *SARS-CoV-2-N-sense* and *SARS-CoV-2-orf1ab* probes reveals no red or blue puncta. Ciliated cells harbor *FOXJ1* puncta. (E) Confocal image of a section

(legend continued on next page)

of the olfactory mucosa of control #15. This negative control for the *SARS-CoV-2-S* and *SARS-CoV-2-orf1ab-sense* probes reveals no red or blue puncta. TUBB3 marks OSNs in the olfactory epithelium and labels OSN axon bundles in the lamina propria. (F) Confocal image of a section of the olfactory bulb of control #15. This negative control for the *SARS-CoV-2-N* and *SARS-CoV-2-S-sense* probes reveals no red or blue puncta. TUBB3 marks axons and olfactory bulb neurons. DAPI served as nuclear stain.

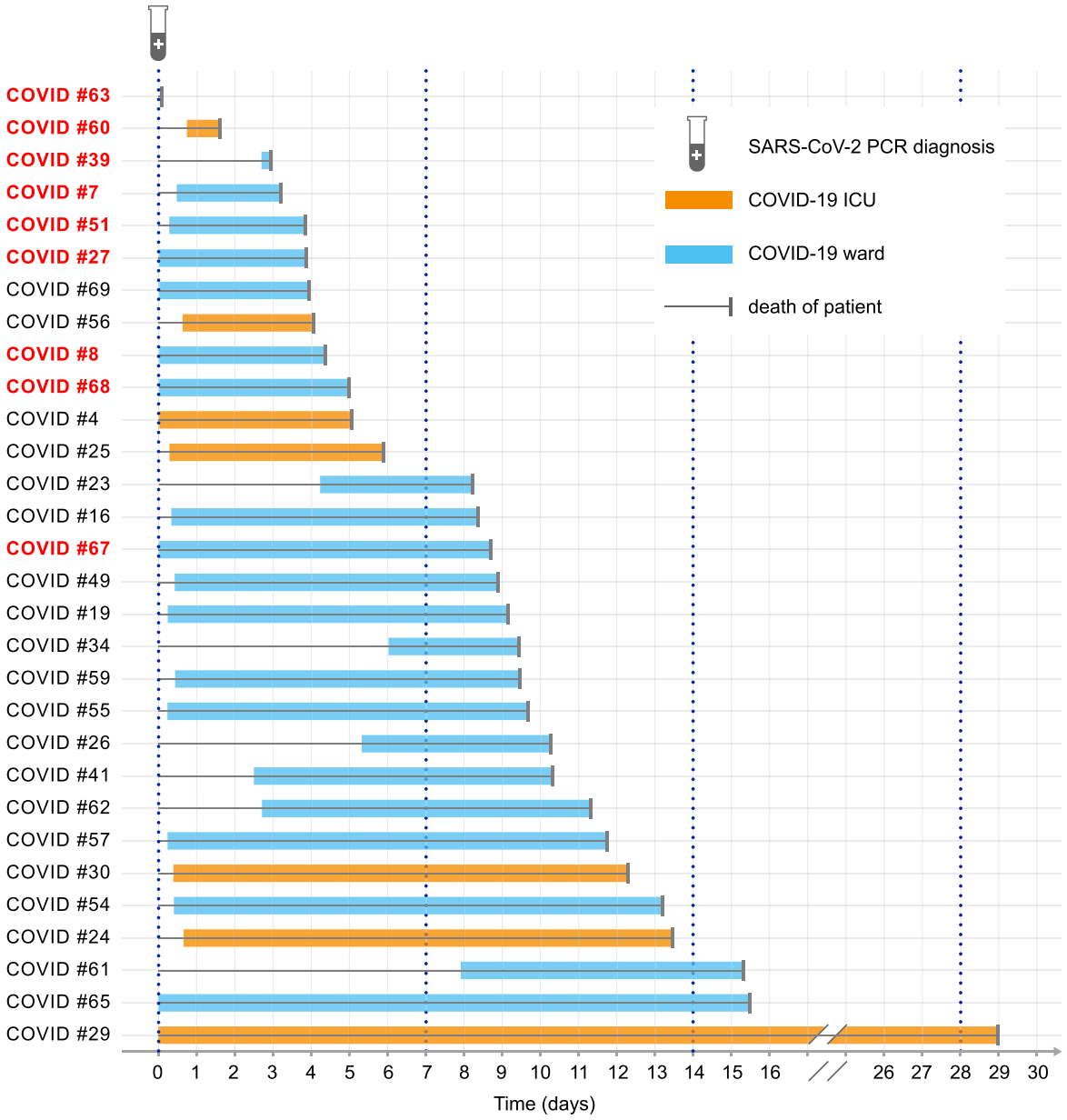

Figure S3. Swimmer plot of the 30 informative COVID-19 cases, related to Figure 1

The definition of "informative case" is based on the detection of *SARS-CoV-2* RNA in the respiratory mucosa by the RNAscope platform of ultrasensitive single-molecule fluorescence *in situ* RNA hybridization. The vertical axis shows the pseudonyms of the cases, with red labels indicating cases with ongoing viral replication at the time of death. The horizontal axis shows the period in days starting from the time the nasopharyngeal swab was taken that led to the diagnosis of COVID-19 by PCR (indicated by a test tube at day 0) until the time of death (indicated by a vertical stop line at the end of a bar). Hospitalization in a COVID-19 unit is indicated by the start of the orange bar (ICU, Intensive Care Unit) or the blue bar (ward).

A

	RAT positive	RAT negative	total
informative	24	3	27
non-informative	7	27	34
total	31	30	61

B

COVID case #	Ct NP swab	RAT NP swab
60	10.5	positive
59	14.7	positive
57	14.9	positive
51	17.5	positive
54	18.2	positive
56	19.2	positive
49	22.2	positive
55	23.4	positive
58	24.5	positive
63	25.0	negative
52	28.7	positive

Figure S4. Results of rapid antigen tests and Ct values of PCR tests on nasopharyngeal swabs taken postmortem and preprocedurally, related to Figure 1

(A) Contingency table comparing rapid antigen test (RAT) results with informative versus non-informative classification based on RNAscope staining. RATs were performed starting with COVID #9. In 27 of the 30 informative cases, a RAT was performed, and in 24 of these (89%) the RAT was scored positive. In 34 of 38 the non-informative cases, a RAT was performed, and in 27 of these (79%) the RAT was scored negative. (B) Ct-values of PCR tests ranked from low (= high viral load) to high (= low viral load) and RAT results from 9 informative cases (median 18.2) and 2 non-informative cases, COVID #58 and COVID #52.

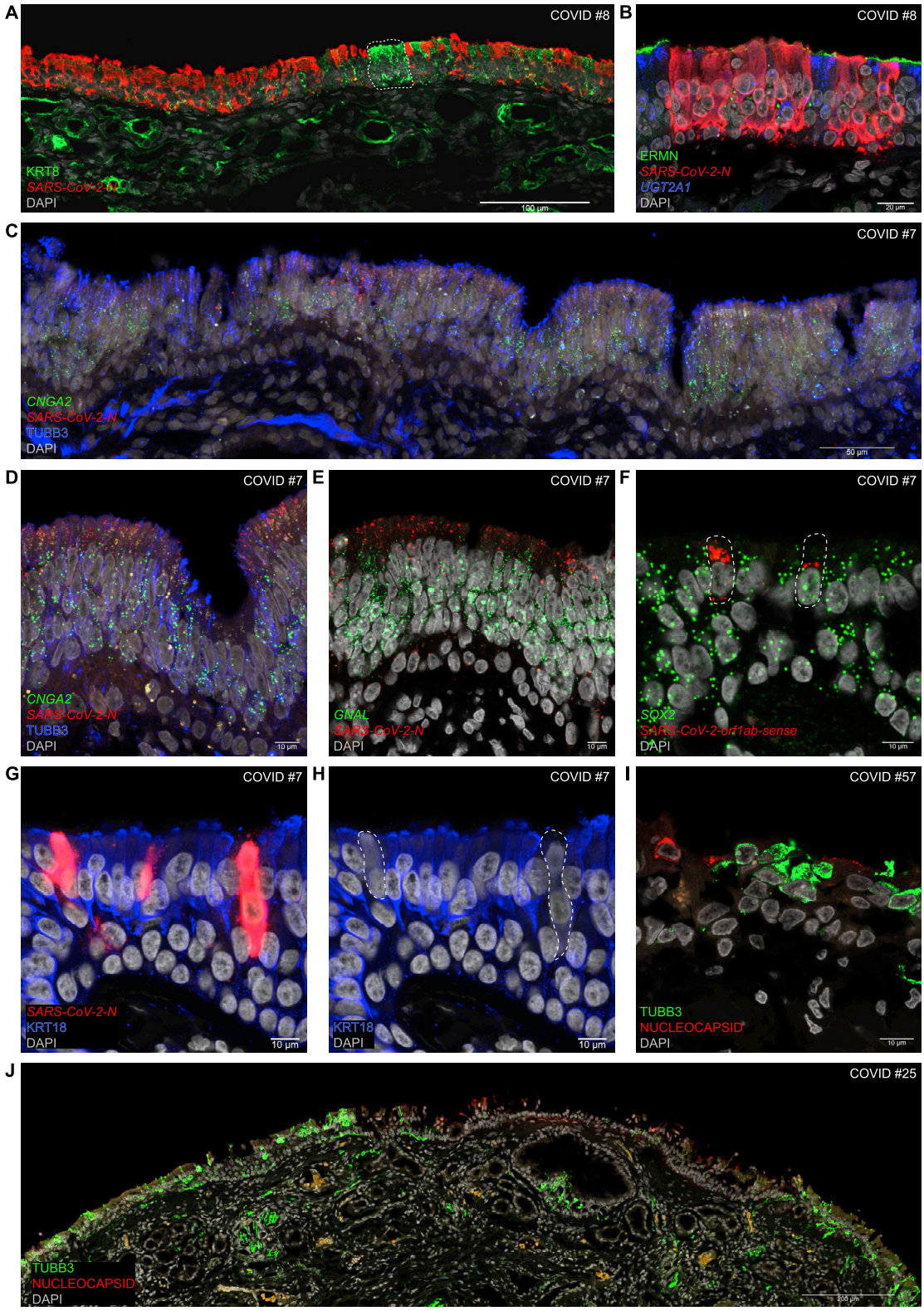

Figure S5. Infection of the olfactory mucosa by SARS-CoV-2, related to Figure 5

Confocal images of sections through the olfactory mucosa of COVID #8 (A and B), COVID #7 (C-H), COVID #57 (I), and COVID #25 (J). (A and B) *SARS-CoV-2-N* puncta occur throughout the apical-basal width of the olfactory epithelium. KRT8-IR signal labels a patch of uninfected sustentacular cells (stippled line) and cells

(legend continued on next page)

lining gland ducts in the lamina propria (A). Infected sustentacular cells are low on or negative for *UGT2A1* puncta and ERMN-IR signal, in contrast to uninfected sustentacular cells (B). (C-E) *SARS-CoV-2-N* puncta occur throughout the apical layer of sustentacular cells, in a mutually exclusive manner with *CNGA2* puncta and TUBB3-IR signal (C and D) or *GNAL* puncta (E) in the middle layer of OSNs. (F) Sustentacular cells harbor *SOX2* puncta across their apical-basal width. The stippled lines outline two sustentacular cells harboring perinuclear *SARS-CoV-2-orf1ab-sense* puncta reflecting ongoing viral replication. (G and H) Three infected sustentacular cells harbor densely packed *SARS-CoV-2-N* puncta, reflecting a high viral load. The stippled lines in H outline two sustentacular cells that are in the plane of focus of this confocal image: their KRT18-IR signal is depleted, in contrast to the strong KRT18-IR signal in nearby uninfected sustentacular cells. (I) Remnants of TUBB3-IR OSNs do not contain nucleocapsid-IR signal. (J) A patch of disintegrating olfactory epithelium containing nucleocapsid-IR signal is flanked by two areas of olfactory epithelium that do not contain nucleocapsid-IR signal but contain numerous TUBB3-IR OSNs.